1 SCIENTIFIC HIGHLIGHT OF THE MONTH

Spin Orbit Driven Physics at Surfaces

M. Heide, G. Bihlmayer, Ph. Mavropoulos, A. Bringer and S. Blügel

Institut für Festkörperforschung
Forschungszentrum Jülich GmbH, D-52425 Jülich

Abstract

The pioneering spintronic proposal of a spin field-effect transistor by Datta and Das motivated largely the research of the spin related behavior of electrons propagating in the potentials with structure inversion asymmetry (SIA). Owing to the spin-orbit interaction, inversion asymmetric potentials give rise to a Bychkov-Rashba spin-orbit coupling causing a spin-splitting of a spin-degenerate electron gas. In this article we show that the rich spin-orbit driven physics in potentials with SIA is effective also for electrons at metallic surfaces. Carrying out first-principles calculations based on density functional theory (DFT) employed in a film full-potential linearized augmented plane-wave (FLAPW) method in which spin-orbit coupling (SOC) is included, we investigate the Rashba spin-splitting of surface electrons at noble-metal surfaces, e.g. Ag(111) and Au(111), at the semimetal surfaces Bi(111) and Bi(110), and the magnetic surfaces Gd(0001) and O/Gd(0001). E.g. on the Bi(110) surface the Rashba spin-splitting is so large that the Fermi surface is considerably altered, so that the scattering of surface electrons becomes fundamentally different. On a magnetic surface, the Rashba splitting depends on the orientation of the surface magnetic moments with respect to the electron wavevector, thus offering a possibility to spectroscopically separate surface from bulk magnetism. Due to the interplay of SIA and SOC effects, magnetic impurities in an electron gas experience spin-spin interactions which arise not only from the common Ruderman-Kittel-Kasuya-Yoshida-type (RKKY) symmetric Heisenberg exchange but in addition also from an Dzyaloshinskii-Moriya-type (DM) antisymmetric exchange. The origin of the latter can be a combination of Moriya-type spin-orbit scattering at the impurities plus kinetic exchange between the impurities and the Fert-Levy type exchange due to relativistic conduction electrons. Assuming that the DM is smaller than the symmetric exchange interaction, we develop a continuum model to explore the rich phase space of possible magnetic structures. Depending on the strength of the DM interaction, we expect in low-dimensional magnets deposited on substrates, such as ultrathin magnetic films, chirality broken two- or three-dimensional magnetic ground-state structures between nanometer and sub-micrometer lateral scale. We present two approaches on how the strength of the DM interaction, the so-called DM vector $\mathbf{D}$, can be calculated from *ab initio* methods, either using the concept of infinitesimal rotations applicable to Green function type electronic structure methods or using the concept of homogeneous spin-spirals more applicable to a supercell type electronic structure method. We determine $\mathbf{D}$ for a doublelayer of Fe on W(110) and show that the quantity is sufficiently large to compete with other interactions. We demonstrate that SOC effects are essential for the understanding of magnetic structures in these ultrathin magnetic films.

1 Introduction

Two independent experiments carried out in 1988 by Albert Fert [1] in Paris and Peter Grünberg in Jülich [2] mark the beginning of *magnetoelectronics* or *spintronics*. In these experiments it was found that an electrical current passing through ferromagnetic films separated by non-magnetic metallic spacer layers is subject to a resistivity which changes by an unexpectedly large amount (gigantic amount at those days) with the change of the relative alignment of the magnetization in these films from ferromagnetic to antiferromagnetic. This observation was coined the giant-magneto-resistance effect or GMR. Obviously GMR made it possible to turn the information of a two-state magnetic configuration (parallel or anti-parallel associated with bit 0 or 1) into an electrical one, or in a more abstract sense, turn spin information into charge current information. Already 8 years after the discovery, this effect is used for example in sensors embodied in read heads in hard disk drives common to all contemporary PCs. Today spintronics is a very active and driving multidisciplinary field whose central theme is the active manipulation of spin-degrees of freedom in solid state systems combining issues of central importance for fundamental physics with great perspectives in applications [3, 4].

Very recently, in the field of *semiconductor spintronics* a number of spin-electronic devices have been proposed, which explicitly make use of the Rashba effect. Here, the basic idea is the control of the spin orientation by utilizing the Rashba spin-orbit coupling [5] utilizing a spin splitting due to spin-orbit coupling in the presence of a structure inversion asymmetric (SIA) potential. This mechanism opens up the possibility to design electronic devices, where the switching process is realized by changing the spin orientation in the semiconductor without application of an external magnetic field. In fact, this scheme is the basis for the well-known spin transistor proposed by Datta and Das [6].

The Datta-Das proposal motivated largely the research of the spin-orbit driven spin splitting in SIA potentials, which turns out to be a rather general phenomenon, and arises not only in two-dimensional electron gases of semiconductor heterostructures but in particular also at (metallic) surfaces and interfaces. Today, the investigation of the spin-orbit coupling of systems with a SIA, provides a subject involving different fields of science including mesoscopic physics, low-temperature physics, surface science, electron spectroscopy, scanning tunneling microscopy (STM) and spectroscopy (STS), nanomagnetism and electronic structure theory. In this article we review at first in section 2 our theoretical first-principles investigations of the Rashba spin-splitting of surface electrons at noble-metal surfaces, e.g. Ag(111) and Au(111), at the semimetal surfaces Bi(111) and Bi(110), and then at magnetic surfaces Gd(0001) and O/Gd(0001). Electrons subjected to the spin-orbit interaction in magnets with a SIA, generate besides the common symmetric Heisenberg-type [7] of exchange, an antisymmetric exchange between spins, known as the Dzyaloshinskii-Moriya (DM) interaction [8, 9] (although the original work was in the context of weak ferromagnetism of insulating antiferromagnetic oxides crystallized in non-centrosymmetric lattices, which relates rather to a Dresselhaus spin-splitting of electrons than to the Rashba spin-splitting, and to a superexchange mechanism rather than that of conduction electrons, for details see below). As we discuss in section 3, the DM interaction destabilizes collinear magnetic structures and favors non-collinear ones. Although about the existence of the DM interaction at surfaces or in nanomagnets cannot be argued in principle, as the reasoning is based on symmetry considerations, after 20 years of intense experimental research in the field of ultrathin magnetic films there are no experimental reports discussing or concluding on the DM interaction in this context. This may suggest that the DM interaction is small and unimportant. In this article we show this is not so. In fact, nobody knows how strong it actually is. We think it is correct to assume that the antisymmetric exchange is smaller than the symmetric one. Then, depending on the strength of the DM interaction, we expect in low-dimensional magnets deposited on substrates, such as ultrathin magnetic films, magnetic ground-state structures with a lateral length scale between nanometer and sub-micrometer. This encouraged us to develop a micromagnetic continuum model, presented in section 4, in which we explore the rich phase space of possible magnetic structures. Which of the possible two- or three-dimensional magnetic phases are realized in nature depends strongly on the strength of the DM interaction. This makes first-principles calculations very valuable. At the same time, the fact that one deals here with magnetic structures of large lateral extent, at surfaces, requiring spin-orbit interaction and structural relaxation makes first-principles calculations a true challenge. This might be the reason why in fact no hard numbers are known for $\mathbf{D}$. In this article we report on two conceptually different approaches to calculate the Dzyaloshinskii-Moriya vector $\mathbf{D}$ from first-principles. In section 5.1, $\mathbf{D}$ is derived in the spirit of the Lichtenstein formula [10] using the concept of infinitesimal rotations. The method is optimally suited for Green-function type electronic structure methods. To calculate $\mathbf{D}$ by wave function based methods we outline in section 5.2 a perturbative treatment of the spin-orbit interaction on top of self-consistently calculated homogeneous periodic spin-spirals. All results are obtained with the full-potential linearized augmented planewave method [11] as implemented in the `FLEUR` code [12]. Our calculations include spin-orbit coupling (SOC) [13] and spin-spirals are implemented in the general context of non-collinear magnetism according to reference [14]. In section 6 we present an example where we actually calculated $\mathbf{D}$ for a Fe double layer on W(110), and discuss the consequences for the magnetic structures of domain walls for that system. At first, we continue with some simple considerations about Rashba spin-spitting due the spin-orbit interaction in SIA, and what it means for the Datta-Das spin-field-effect transistor. A motivation to study these effects is to translate these concepts to the physics of nanostructures at surfaces.

1.1 Rashba Effect

In order to look in more detail into the principles of the Rashba effect in semiconductors we consider a two-dimensional electron gas (2DEG) as it develops typically in epitaxially grown III-V quantum-well heterojunctions shown for example in figure 1. Considering the 2DEG in a constant potential e.g. $V_0 = 0$, neglecting electron correlation and working in a single-particle picture, in the absence of internal and external magnetic fields, $B = 0$, then the motion of the electrons is described by the simple kinetic energy Hamiltonian $H_\mathrm{K} = \frac{\mathbf{p}^2}{2m^*}$. p is the momentum operator and m^* are the masses of the valence or conduction band electrons, respectively. The single particle energy $\varepsilon(\mathbf{k}) = \frac{\hbar^2}{2m^*}\mathbf{k}^2$ depends on the Bloch vector $\mathbf{k}$, indicating the orbital motion of the eigenstate, which is a plane wave $\psi_\mathbf{k}(\mathbf{r}) = \frac{1}{\sqrt{\Omega}}e^{i\mathbf{kr}}$. Each eigenstate $\varepsilon_{\uparrow\downarrow}(\mathbf{k})$ is two-fold degenerate for spin-up and spin-down electrons which is a combined consequence of inversion symmetry of space and time. Space inversion symmetry changes the wave vector

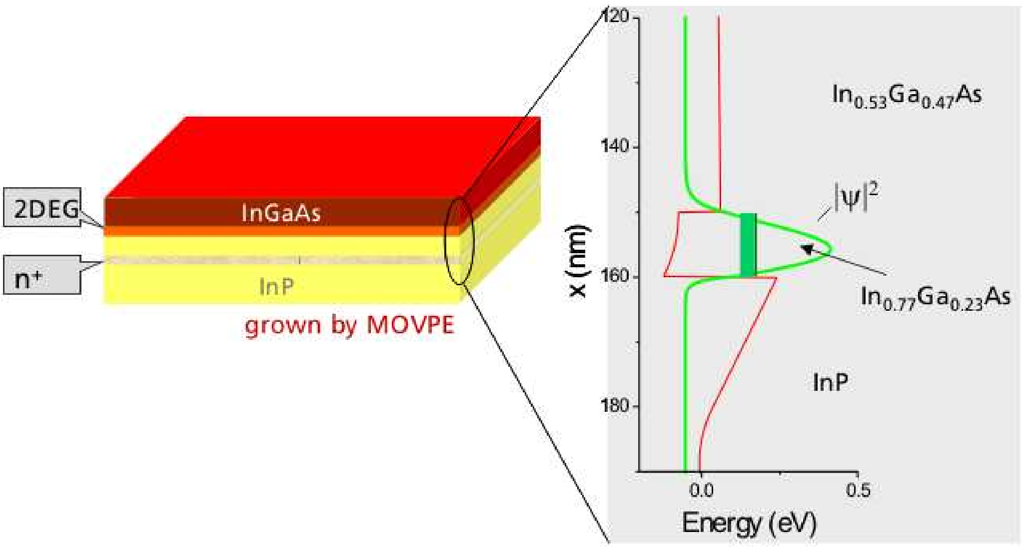

Figure 1: Schematic illustration of a $\mathrm{In_{0.53}Ga_{0.47}As/In_{0.77}Ga_{0.23}As/InP}$ heterostructure. The two-dimensional electron gas is located in the strained $\mathrm{In_{0.77}Ga_{0.23}As}$ layer. Such a heterostructure is typically grown by metal-organic vapor phase epitaxy on a semi-insulating InP substrate. The two-dimensional electron gas (2DEG) is located in a strained 10 nm thick $\mathrm{In_{0.77}Ga_{0.23}As}$ layer. The lower barrier of the quantum well is formed by an InP layer, while for the upper layer a 70 nm thick $\mathrm{In_{0.53}Ga_{0.47}As}$ layer is used. The electrons are provided by a 10 nm thick InP dopant layer separated by 20 nm of InP from the quantum well [15].

$\mathbf{k}$ into $-\mathbf{k}$ and for each spin-direction σ, $\sigma \in \{\uparrow, \downarrow\}$, the single-particle energy transforms as $\varepsilon_\sigma(\mathbf{k}) = \varepsilon_\sigma(-\mathbf{k})$. Time inversion symmetry flips in addition the spin, i.e. $\varepsilon_\uparrow(\mathbf{k}) = \varepsilon_\downarrow(-\mathbf{k})$, known as the Kramers degeneracy of the single-particle states. Thus, when both symmetry operations are combined we obtain the two-fold degeneracy of the single-particle energies, $\varepsilon_\uparrow(\mathbf{k}) = \varepsilon_\downarrow(\mathbf{k})$. When the potential through which the carriers move is inversion-asymmetric as in the example of the strained heterojunction in figure 1, then the spin-degeneracy is removed even in the absence of an external magnetic field $\mathbf{B}$. Performing a Taylor expansion of the potential $V(\mathbf{r})$, $V(\mathbf{r}) = V_0 + e\mathbf{E}\cdot\mathbf{r} + \cdots$, in lowest order the inversion asymmetry of the potential $V(\mathbf{r})$ is characterized by an electric field $\mathbf{E}$. When electrons propagate with a velocity $\mathbf{v} = d\varepsilon/d\mathbf{p} = \frac{\hbar}{m^*}\mathbf{k}$ in an external electric field $\mathbf{E}$ defined in a global frame of reference, then the relativistic Lorentz transformation gives rise to magnetic field $\mathbf{B} = \frac{1}{c}\mathbf{v}\times\mathbf{E} = \frac{\hbar}{m^* c}\mathbf{k}\times\mathbf{E}$ in local frame of the moving electron. The interaction of the spin with this $\mathbf{B}$ field leads then to the Rashba or Bychkov-Rashba Hamiltonian [16, 17]

$$H_\mathrm{R} = \frac{\alpha_\mathrm{R}}{\hbar}\boldsymbol{\sigma}(\mathbf{p}\times\mathbf{E}) \qquad \text{or} \qquad H_\mathrm{R} = \alpha_\mathrm{R}\,\boldsymbol{\sigma}(\mathbf{k}\times\mathbf{E}) \qquad \text{or} \qquad H_\mathrm{R} = \alpha_\mathrm{R}(|\mathbf{E}|)\,\boldsymbol{\sigma}(\mathbf{k}\times\hat{\mathbf{e}}) \tag{1}$$

describing the Rashba spin-orbit coupling as additional contribution to the kinetic energy. $\boldsymbol{\sigma} = (\sigma_x, \sigma_y, \sigma_z)$ are the well-known Pauli matrices. The latter two terms are strictly correct only for plane wave eigenstates as for the 2DEG. α_R denotes a materials-specific prefactor, known as Rashba parameter. Different definitions exist, also that for which the strength of the $\mathbf{E}$-field, $|\mathbf{E}|$, is included in $\alpha_\mathrm{R}(|\mathbf{E}|)$ and only the direction of $\mathbf{E}$, $\hat{\mathbf{e}}$, enters the Hamiltonian. This Hamiltonian leads then to the structure inversion-asymmetric (SIA) spin splitting, the Rashba effect [5, 16, 17]. Today, it is common practice to use the term *Rashba-effect* both for the Hamiltonian given in equation (1) as well as for the SIA spin splitting in general.

Although we have motivated the Rashba Hamiltonian heuristically by a Lorentz transformed confining external electric field, in general the Rashba parameter α_R is not directly proportional to it. Instead a microscopic view is required and the effect is caused by the spin-orbit interaction as described in a Pauli-like (or scalar-relativistic equation plus spin-orbit interaction as for *ab initio* calculations, c.f. subsection 2.1) equation (15), which takes care on the Lorentz transformation locally of the moving electron of quantum number $\mathbf{k}$ in the structure inversion-asymmetric potential. Then, the strength of SIA spin splitting depends on the asymmetry of the electronic structure on the spin-orbit matrix elements, most prominently on the asymmetry of the penetration of the electron wave functions into the barrier, but also on the orbital character, the size of the band gap and the atomic spin-orbit strength which scales typically quadratically with the nuclear number Z. Electronic structure $\mathbf{k}\cdot\mathbf{p}$ calculations of α_R can be found in the book of Winkler [18] and references therein.

The general features of the Rashba-model are studied for the 2DEG in a SIA potential and the solution is displayed schematically in figure 2. For electrons propagating in the 2DEG extended in the $(x,\,y)$ plane subject to an electric field normal to the 2DEG, $\hat{\mathbf{e}}_z = (0,0,1)$, the Hamiltonian takes the form

$$H = H_\mathrm{K} + H_\mathrm{R} = \frac{\mathbf{p}_\parallel^2}{2m^*} + \frac{\alpha_\mathrm{R}}{\hbar}\left(\boldsymbol{\sigma}\times\mathbf{p}_\parallel\right)_{|z} = \frac{\mathbf{p}_\parallel^2}{2m^*} + \frac{\alpha_\mathrm{R}}{\hbar}\left(\sigma_x p_y - \sigma_y p_x\right), \tag{2}$$

which is solved analytically. For a Bloch vector in the plane of the 2DEG, $\mathbf{k}_\parallel = (k_x, k_y, 0) = k_\parallel(\cos\varphi, \sin\varphi, 0)$, the eigenstates written as a product of plane wave in space and two-component spinor are

$$\psi_{\pm\mathbf{k}_\parallel}(\mathbf{r}_\parallel) = \frac{e^{i\mathbf{k}_\parallel\cdot\mathbf{r}_\parallel}}{2\pi}\frac{1}{\sqrt{2}}\begin{pmatrix} ie^{-i\varphi/2} \\ \pm e^{i\varphi/2}\end{pmatrix} \tag{3}$$

with eigenenergies

$$\varepsilon_\pm(\mathbf{k}_\parallel) = \frac{\hbar^2}{2m^*}\mathbf{k}_\parallel^2 + \alpha_\mathrm{R}\left(\boldsymbol{\sigma}\times\mathbf{k}_\parallel\right) = \frac{\hbar^2}{2m^*}\mathbf{k}_\parallel^2 \pm \alpha_R|\mathbf{k}_\parallel| = \frac{\hbar^2}{2m^*}(k_\parallel \pm k_\mathrm{SO})^2 - \Delta_\mathrm{SO}\,, \tag{4}$$

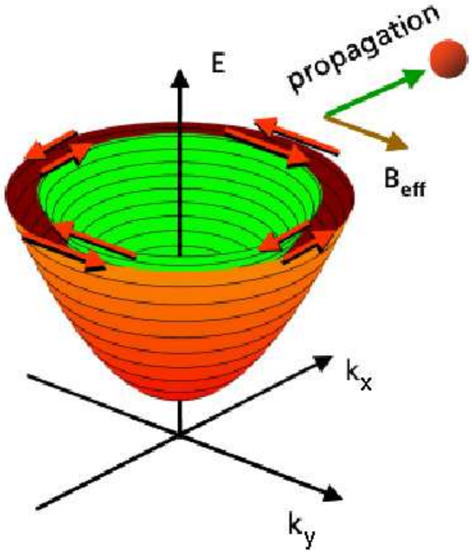

Figure 2: Parabolic energy dispersions of a two-dimensional electron gas in a structure inversion asymmetric (SIA) environment. Indicated are the vector fields of the spin-quantization axes (or the patterns of the spin) at the Fermi surface. As the opposite spins have different energies, the Fermi surface becomes two concentric circles with opposite spins. The effective B-field, $\mathbf{B}_\mathrm{eff}$ is perpendicular to the propagation direction defined by $\mathbf{k}_\parallel$.

where ± denotes the spin-up and -down states with respect to a spin orientation axis $\hat{\mathbf{n}}(\mathbf{k}_\parallel)$, local in $\mathbf{k}_\parallel$ space. With the exception of the high-symmetry state $k_\parallel = 0$, we find that the original two-fold degenerate energy paraboloid of the 2DEG in a constant potential indeed spin-splits. The spin splitting $\varepsilon_+(\mathbf{k}_\parallel) - \varepsilon_-(\mathbf{k}_\parallel) = 2\alpha_r k_\parallel$ is linear in $k_\parallel$. Due to the presence of the SIA potential and the spin-orbit interaction, the origin of the degenerate parabola is shifted by $k_{\mathrm{SO}} = m^*\alpha_R/\hbar^2$, but in opposite directions for up- and down-spins with in overall spin-orbit lowering of $\Delta_{\mathrm{SO}} = m^*\alpha_R/(2\hbar^2)$. The orientation axis is given by the expectation value

$$\hat{\mathbf{n}}_\pm(\mathbf{k}_\parallel) = \langle \psi_{\pm\mathbf{k}_\parallel} | \boldsymbol{\sigma} | \psi_{\pm\mathbf{k}_\parallel} | \rangle = \pm \begin{pmatrix} \sin\varphi \\ -\cos\varphi \\ 0 \end{pmatrix} \quad \perp \quad \mathbf{k}_\parallel = k_\parallel \begin{pmatrix} \cos\varphi \\ \sin\varphi \\ 0 \end{pmatrix} . \tag{5}$$

We find that the orientation axis is independent of the magnitude $k_\parallel$ and depends only on the direction of the $\mathbf{k}_\parallel$ vector. In fact, it is in the plane of the 2DEG and the orientation axis is perpendicular to the propagation direction of the electron. Considering $\mathbf{k}_\parallel \to -\mathbf{k}_\parallel$, φ changes to $\varphi + \pi$, we find that the spin orientation axis reverses. $\hat{\mathbf{n}}_\pm(\mathbf{k}_\parallel) \to \hat{\mathbf{n}}_\mp(-\mathbf{k}_\parallel) \to -\hat{\mathbf{n}}_\pm(-\mathbf{k}_\parallel)$. Thus for $\mathbf{k}_\parallel$ and $-\mathbf{k}_\parallel$ the spin-up and -down states refer to opposite orientations. Defining a global quantization axis along the line $(-\mathbf{k}_\parallel, \mathbf{k}_\parallel)$, e.g. according to $\hat{\mathbf{n}}_\pm(+\mathbf{k}_\parallel)$, then a spin-up state appears as spin-down state if $\mathbf{k}_\parallel$ changes sign. Together with the eigenvalue spectrum given in equation (4) the Kramer degeneracy $\varepsilon_\uparrow(\mathbf{k}_\parallel) = \varepsilon_\downarrow(-\mathbf{k}_\parallel)$ holds. In all, the magnetic moment is zero when averaged over all states $\mathbf{k}_\parallel$. This is consistent with the absence of an $\mathbf{B}$ field. The Rashba spin-orbit splitting may be observed either by electron photoemission or transport experiments. In both cases experiments have to be carried out at temperatures, k_BT which are lower than the energy difference of the spin-splitting, $\varepsilon_+(\mathbf{k}_\parallel) - \varepsilon_-(\mathbf{k}_\parallel)$. In angle resolved photoemission the eigenvalue spectrum is measured for a selected $\mathbf{k}_\parallel$ value. Two peaks at different energies are expected. Using spin-polarization analysis, for example using a Mott-detector oriented perpendicular to the propagation direction of the electron, different polarizations should be observed for the two peaks. Transport experiments work typically on a shell of constant energy ε. Here we expect at a given energy two different wave vectors for up- and down-electrons, which will be exploited in the Datta-Das proposal of a spin-transistor.

That the Pauli-like spin-orbit coupling may have important consequences for the one-electron energy levels in bulk semiconductors was first emphasized by Dresselhaus *et al.* [19] already in 1955. Unlike the diamond structure of Si and Ge, the zinc blende structure, in which for example the III-V semiconductor crystallize, exhibit a bulk inversion asymmetry (BIA), i.e. this crystal structure lacks a center of inversion, so that we can have a spin splitting of the electron and hole states at nonzero wave vectors $\mathbf{k}$ as for the Rashba effect even if $\mathbf{B} = 0$. Today, this is called the Dresselhaus effect. The corresponding Dresselhaus Hamiltonian

$$H_{\mathrm{D}} = \frac{\alpha_{\mathrm{D}}}{\hbar} \left[\sigma_x p_x \left(p_y^2 - p_z^2\right) + \sigma_y p_y \left(p_z^2 - p_x^2\right) + \sigma_z p_z \left(p_x^2 - p_y^2\right)\right] \tag{6}$$

describes the BIA spin splitting due to the Dresselhaus spin-orbit coupling, which produces spin vector fields quite different from those produced by the SIA splitting. One difference is obviously that the Dresselhaus term produced a spin splitting which is proportional to k^3, $\varepsilon_{\mathrm{D}} \propto k^3$, while the spin splitting of the Rashba-term is linear in k, $\varepsilon_{\mathrm{R}} \propto k$. Since we focus in this article on spin-orbit driven physics of SIA potentials this term is not further considered.

1.2 Datta-Das Spin Field Effect Transistor

Figure 3 explains the Datta-Das [6] proposal of a spin field-effect transistor (SFET) exploiting the Rashba effect. What is remarkable about this theoretical transistor model is the fact that the tuning of the precessing spin-orientation is accomplished by applying an electric rather than a magnetic field. Considering the fact that in semiconductor devices it is much easier to generate electric fields as to integrate externally controllable magnetic fields, this paves a way to even more complex devices.

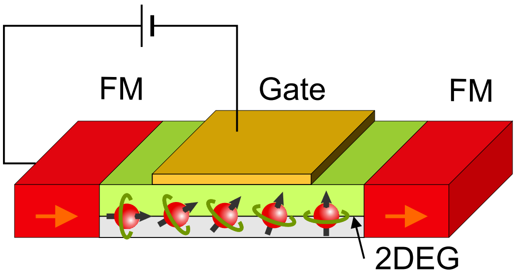

Figure 3: Scheme of the Datta-Das spin field-effect transistor (SFET). The source (spin injector) and the drain (spin detector) are ferromagnetic metals or semiconductors, with parallel alignment of magnetic moments. The injected spinpolarized electrons with wave vector **k** move ballistically through the 2DEG (which is actually quantized along a quasi-one-dimensional channel) formed by, for example, a strained InGaAs/InP heterojunction. While propagating from source to drain, electron spins precess about a precession axis, which arises from spin-orbit interaction, which is defined by the structure and the materials properties of the channel. The change of the precession angle with propagation distance is tunable by the gate voltage. The current is large if the electron spin at the drain points in the initial direction, and small if the direction is reversed. Shown is an intermediate situation. For simplicity we call the left ferromagnet the source, which acts as spin injector and the right ferromagnet the drain, which acts as spin analyzer.

To understand the principle of the Datta-Das transistor we consider again a 2DEG in the semiconductor part of the transistor located in the x-y-plane, while the quantum-well potential, as well as the variable gate voltage, are orientated along the z-axis. We develop a simple one-dimensional model. The x-axis is the direction of propagation for the electrons and at the same time the polarization axis of the ferromagnetic source and drain. As we have seen in subsection 1.1, the direction of propagation defined by $\mathbf{k}_\parallel$ determines the spin orientation $\hat{\mathbf{n}}$ of the eigenstates in the 2DEG, which is in the plane of the 2DEG pointing perpendicular to the propagation direction, which is the y and $-y$ direction in our frame of reference, i.e. $\mathbf{k}_\parallel = (k_x, 0, 0)$, $\varphi = 0$ and $\hat{\mathbf{n}} = \pm(0, 1, 0)$, taken the definitions entering equation (5). Neglecting the spatial plane wave prefactor, according to equation (3) the eigenstates with respect to this quantization axis take the form $|\uparrow\rangle = \frac{1}{\sqrt{2}}(i, 1)$ and $|\downarrow\rangle = \frac{1}{\sqrt{2}}(i, -1)$. An electron at the point of injection into the 2DEG next to the ferromagnetic injector is not in an eigenstate, because both spin and propagation vector point in the same direction. But its spinor quantized along the x

direction, $| \rightarrow\rangle = \frac{1}{\sqrt{2}}(1,1)$ can be expressed in terms of above eigenstate as

$$| \rightarrow\rangle = \frac{1}{\sqrt{2}}\begin{pmatrix} 1 \\ 1 \end{pmatrix} = \frac{1}{2}\left[(1-i)\frac{1}{\sqrt{2}}\begin{pmatrix} i \\ 1 \end{pmatrix} + (-1-i)\frac{1}{\sqrt{2}}\begin{pmatrix} i \\ -1 \end{pmatrix}\right]. \tag{7}$$

Taking into consideration that the eigenstates propagate as plane waves along the x-axis, the x-dependent amplitude $\psi(x)$ of the injected electron of fixed energy ε

$$\psi(x) = \frac{1}{2}\left[(1-i)e^{ik_\uparrow x}| \uparrow\rangle + (-1-i)e^{ik_\downarrow x}| \downarrow\rangle\right] \tag{8}$$

is a coherent superposition of up- and down-states. The values $k_\uparrow$, $k_\downarrow$ belong to the opposing spin states at fixed energy ε and can be obtained from equation (4)

$$k_{\uparrow,\downarrow} = \kappa \mp k_{\mathrm{SO}} \qquad \text{with} \qquad \kappa = \sqrt{\frac{2m^*}{\hbar}\varepsilon + k_{\mathrm{SO}}^2}\,. \tag{9}$$

Substituted back into equation (8), this gives the wave function the final form

$$\psi(x) = \left(\cos(k_{\mathrm{SO}}x)| \rightarrow\rangle \;-\; \sin(k_{\mathrm{SO}}x)| \leftarrow\rangle\right)\,. \tag{10}$$

The expression includes the spinor eigenstates in x and $-x$ direction. Here we can see for which particular channel length L between the injector and analyzer, the spin is parallel ($k_{\mathrm{SO}} = n\pi/L$) or antiparallel ($k_{\mathrm{SO}} = (n+1/2)\pi/L$) to the magnetization direction of the ferromagnetic analyzer. By calculating the spin orientation axis

$$\hat{\mathbf{n}} = \langle\psi(x)|\boldsymbol{\sigma}|\psi(x)\rangle = \begin{pmatrix} \cos(2k_{\mathrm{SO}}x) \\ 0 \\ -\sin(2k_{\mathrm{SO}}x) \end{pmatrix} \tag{11}$$

we see that the spins precess in the x-z plane. The wavelength of precession $\lambda = \pi/k_{\mathrm{SO}} = \pi\hbar^2/(m^*\alpha_R(E_z))$ depends on the electric field E_z and it should in principle be possible to tune E_z such that either full- or half-integer spin revolutions fit into the gate length L. The spin-precession has also a classical analogon: a electron with a magnetic spin moment m_x pointing into the x-direction is injected into the 2DEG and is subject to an Rashba B_y-field in the y direction. Thus, a torque $\boldsymbol{\tau} = \mathbf{m} \times \mathbf{B}$ is exerted on the magnetic moment which gives rise to a precession of the moment in the x-z plane.

1.3 Spin structure in quantum wires

In the geometry of the SFET (figure 3) the motion of the electrons is restricted to one preferred direction (x). Orthogonal to this direction (y) the wave functions are bound by a wall like potential (cf. figure 4). The lack of circular symmetry causes a non trivial spin distribution across the wire. This may be shown by solving the Schrödinger equation

$$\left(H_K + H_R + V\right)\Psi = \mathcal{E}\Psi$$

with the Hamiltonian of eqn. (2) and a confining Potential V in y-direction. For a long wire the wave functions are separable

$$\Psi = \begin{pmatrix} \psi_+ \\ \psi_- \end{pmatrix} = e^{ik_x x}\begin{pmatrix} f\,(y) \\ ig\,(y) \end{pmatrix}. \tag{12}$$

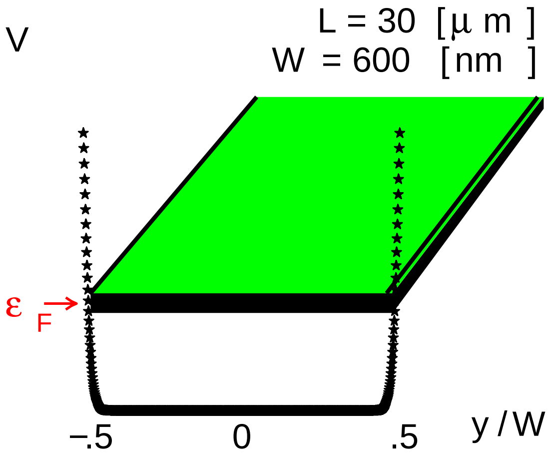

Figure 4: Schematic picture of a quantum wire made out of the heterostructure material of figure 1. The typical width W and length L and position of the Fermi energy ϵ_F are indicated.

With the scaled quantities $y = Ws$, $\kappa = Wk_x$, $\eta = \alpha_R m^* W/\hbar^2$, $\epsilon = m^*(W/\hbar)^2\mathcal{E}$, $v = m^*(W/\hbar)^2 V$, this results in two coupled differential equations for the spinor functions f and g:

$$\left[-\frac{1}{2}\left(\frac{d}{ds}\right)^2 + \frac{1}{2}\kappa^2 + v - \epsilon\right]\left(\begin{array}{c} f \\ g \end{array}\right) = \left[\begin{array}{cc} 0 & \eta\left(\kappa - \frac{d}{ds}\right) \\ \eta\left(\kappa + \frac{d}{ds}\right) & 0 \end{array}\right]\left(\begin{array}{c} f \\ g \end{array}\right). \qquad (13)$$

They may be solved by standard discretization methods [20]. A typical wave function is shown in the right of figure 5. In a wire a fraction of the kinetic energy rests in the confinement. One observes wave functions with increasing number of nodes across the wire at higher energies. The local spin direction is defined by

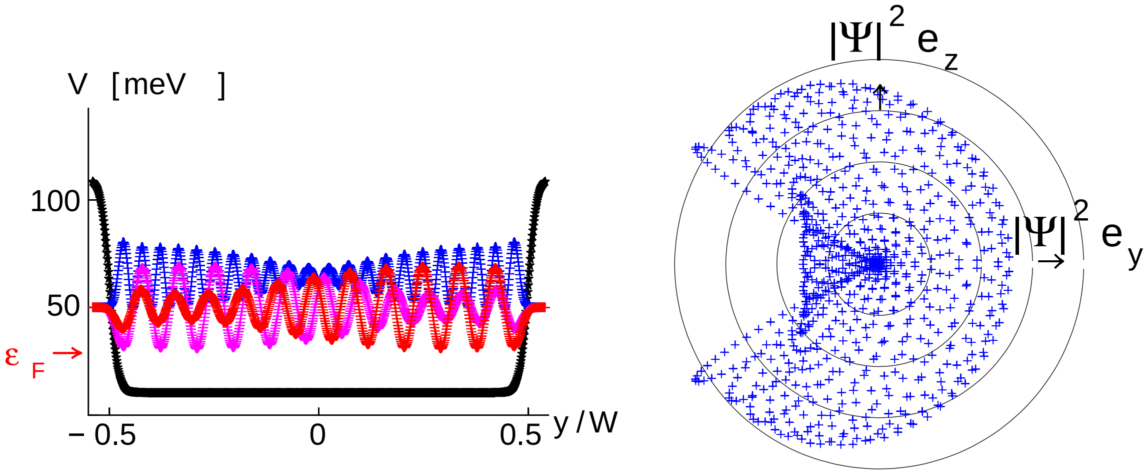

Figure 5: Left: Spinor wave functions (f red, g purple) and density (blue) at ϵ_F across the wire of figure 4. Right: Polar plot of the spin direction across the wire of the wave function shown in the left part.

$$(e_x, e_y, e_z) = \left(0\ ,\ \frac{2fg}{f^2+g^2}\ ,\ \frac{f^2-g^2}{f^2+g^2}\right) \qquad (14)$$

and may be plotted weighted by the density in a polar diagram (right of figure 5). From left to right, the spin direction is turned from the lower to the upper side of the wire plane. This left right asymmetry is present in most of the stationary states and there have been attempts to observe it experimentally [21].

2 The Rashba effect at metallic surfaces

2.1 Nonmagnetic Surfaces

A surface state can be considered as a particular realization of a two dimensional electron gas. Since the surface always breaks spatial inversion symmetry, the effective potential which acts on the surface state will generally have a finite gradient along the surface normal, i.e. there is an electric field in this direction. The physical manifestation of this field is the workfunction.

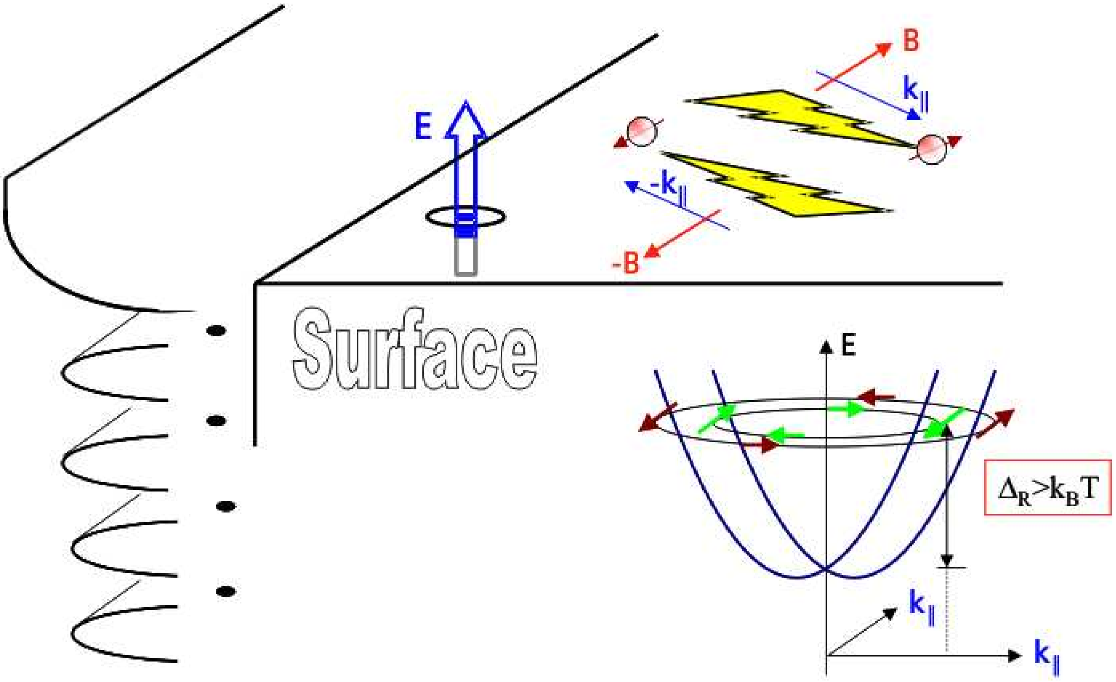

Figure 6: Electrons moving with in-plane wavevectors $\mathbf{k}_\parallel$ and $-\mathbf{k}_\parallel$ in the potential gradient of a surface (indicated on the left). The resulting electric field, $\mathbf{E}$, is seen in the restframe of the moving electrons as a magnetic field $\mathbf{B}$ or $-\mathbf{B}$ which couples to the spin of the electron. This interaction modifies the bandstructure of a spin-degenerate (s, p_z)-like surface state as shown in the lower right picture. The degeneracy is lifted and the electrons at the Fermi level have spin directions perpendicular to their propagation directions as indicated by the small arrows (cf. also preceding section).

Like in the semiconductor heterostructures discussed above, due to the movement of an electron with wavevector $\mathbf{k}_\parallel$ in the surface plane, this electric field appears in the rest frame of the electron as a magnetic field which couples to the spin of the electron. The situation is schematically depicted in figure 6 for two electrons traveling on the surface in opposite directions. For a non-spinpolarized surface state (e.g. on a nonmagnetic surface) this gives rise to a term in the

Hamiltonian

$$H_{\mathrm{soc}} = \frac{\hbar}{4m_{\mathrm{e}}^2c^2}\boldsymbol{\sigma}\cdot(\nabla V(r)\times\mathbf{p}) \tag{15}$$

which leads to a k-dependent splitting of the dispersion curves. When we simply use the nearly free electron gas (NFEG) model and substitute $\mathbf{p}$ by the $\mathbf{k}$-vector, for usual workfunctions we would expect this splitting to be very small, in the order of 10^{-6} eV. This would be far too small to observe directly with angle resolved photoemission spectroscopy (ARPES). So it came rather as a surprise, when in 1996 LaShell and coworkers [22] discovered a splitting of the surface state of the Au(111) surface, which was not only k-dependent, but also in the order of 0.1 eV at the Fermi level. They correctly interpreted this splitting as a spin-orbit coupling effect, which obviously was influenced by the strong atomic spin-orbit effects in the heavy Au atom. Spin resolved ARPES experiments finally also analysed the spin distribution of this surface state [23] and found it to be in quite good agreement with the NFEG model (cf. figure 6), as it was also predicted theoretically [24].

While this effect was observed in different studies for the Au(111) surface, on other surfaces which show a similar Shockley state, e.g. Ag(111) or Cu(111), no such splitting was discovered experimentally and in calculations [25] based on density functional theory (DFT). From the calculations it was concluded, that the k-dependent splitting on Ag(111) is by a factor 20 smaller than on Au(111) (cf. also figure 7). This can neither be explained by the difference in atomic spin-orbit coupling of Au ($Z = 79$) and Ag ($Z = 47$) alone, nor by the potential gradients at the surface. Also the amount of p-character in the sp-surface state is larger for Ag than for Au, so that in principle spin-orbit effects should be more prominent in silver. So what is responsible for the size of the effect?

To resolve this issue, we did calculations based on DFT with the full potential linearized augmented planewave method [11] as implemented in the FLEUR code [12]. Our calculations include spin-orbit coupling (SOC) in a self-consistent manner [13] in the muffin-tin (MT) spheres. For the present discussion it might be interesting to note, that actually only the spherically symmetric part of the potential is included in the calculations, which might seem inconsistent with the above discussion which claims that the potential gradients at the surface are responsible for the effect we want to describe. But we will see, that in all considered cases the agreement with experimental data is fine, suggesting that the theoretical approach includes the dominant terms leading to the Rashba-type splitting in question.

In the calculations we can choose the region where to include SOC: in specific spheres around the atoms, i.e. in certain layers of the film, or we can also vary the size of the sphere, where we want to include spin-orbit coupling. In this way, it is possible to show that a bit less 60% of the k-dependent splitting of the Au(111) surface state comes from the surface layer and the contribution in deeper layers decays more or less like the weight of the surface state in these layers [26]. Moreover, this effect is extremely localized in the core region, where the *radial* potential gradient is largest. For Au(111), more that 90% of the effect originate from a sphere with radius 0.25 a.u. around the nucleus. In this region the potential is almost perfectly spherically symmetric, so that our above mentioned approximation, to include only the $l = 0$ part of the potential, is probably well justified. The potential gradient at the surface enters actually only indirectly, via the asymmetry of the wavefunction in the core region. In a tight-binding model, Petersen and Hedegård showed that the size of the Rashba-type splitting is determined by the product of the atomic spin-orbit coupling parameter and a measure for the asymmetry of the wavefunction under consideration [27].

A measure for the asymmetry of the wavefunction of a surface state can be found by analysing the l-like character of the state, i.e. to determine how much s, p or d character a surface state shows at a certain $\mathbf{k}_{\|}$-point, in our case the $\overline{\Gamma}$-point. E.g. a surface state of pure p_z character is inversion symmetric and will – in absence of an electric field – show no Rashba-type splitting. The potential gradient or electric field at the surface will distort the wavefunction, so that some s or d_{z^2} contributions to the surface state will arise. The ratio of l- to $l \pm 1$-type character of a surface state (for a given m, e.g. $m = 0$) will therefore give a measure for the asymmetry of this state. In the case of Ag(111), we find that the surface state is predominantly of p_z-type, with a small d_{z^2} admixture ($p : d$ ratio of 9.5) while in Au the surface state has much stronger d_{z^2} character ($p : d = 3.3$). The fact that the Au d band lies much higher in energy than the Ag d band leads to a stronger d character of the Au surface state and thus to larger asymmetry of the wavefunction [26]. This determines the stronger k-dependent splitting in the Au(111) surface bandstructure.

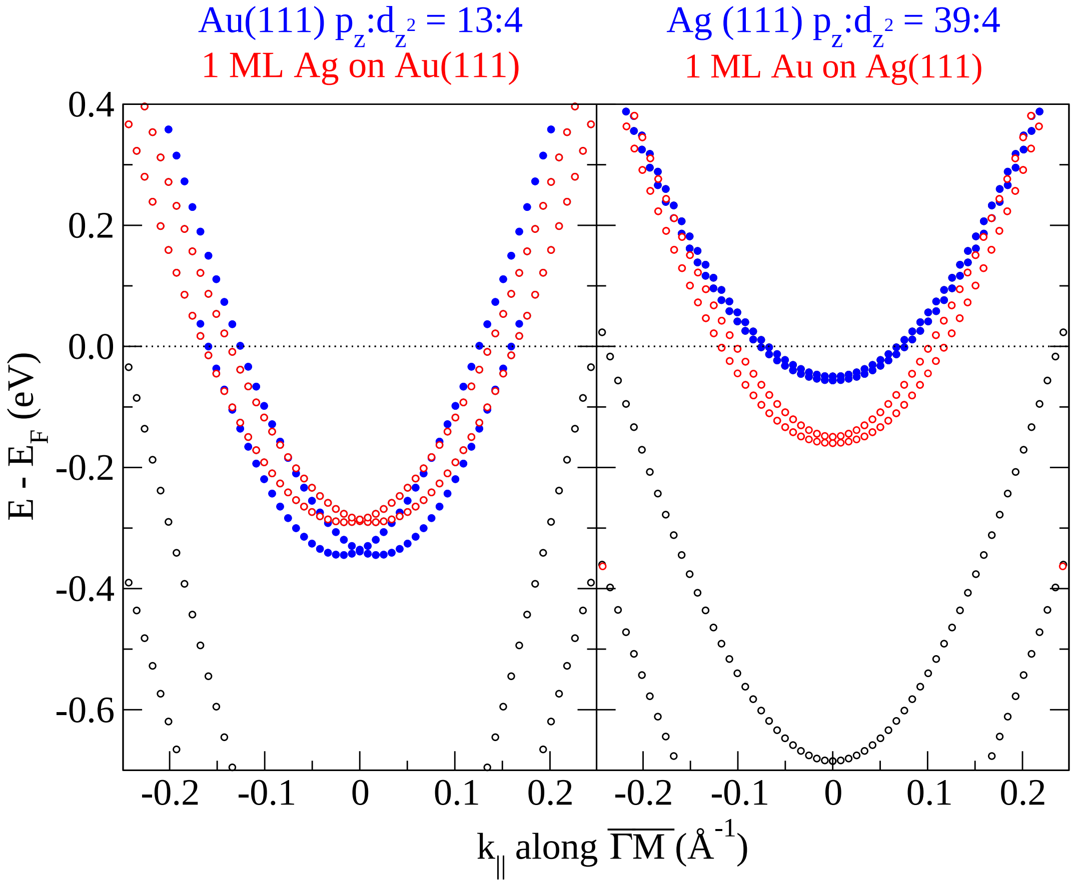

Figure 7: Bandstructure of Au(111) (left, full circles) and one monolayer Ag on Au(111) (left, open circles) as compared to a Ag(111) film (right, full symbols) and a single Au monolayer on Ag(111) (right, open symbols).

This effect can be further demonstrated, when we compare a single monolayer of Ag on Au(111) with a Au monolayer on Ag(111). Just from the point of view of the atomic SOC, we would expect that the Rashba-type splitting of the Au monolayer of Ag(111) is larger than that of the Ag/Au(111) system, since more than 50% of the effect comes from the surface layer. But since the gold d states of the subsurface layers can induce a larger d character of the Ag surface state in Ag/Au(111) while the Au surface state of Au/Ag(111) has less d character than the one of pure Au(111), finally the Rashba-type spin-orbit splitting is larger in Ag/Au(111) (cf. figure 7). Other examples, how the asymmetry of a surface state influences the strength of the Rashba-type splitting can be found on lanthanide surfaces (e.g. Lu(0001) [26]), and a particular case will be presented in subsection 2.3.

2.2 Semimetal Surfaces

Up to now we have discussed examples, where the Rashba-type spin-orbit splitting was in the order of 10 to 100 meV (up to 120 meV for Au(111)), so that experimentally it is not so easy to detect in ARPES experiments. Now, we turn to another extreme, where the splitting is so big, that it was not a-priori clear, whether the two experimentally observed features were spin-split partners of the same state or two different surface states: the low-index surfaces of Bi. Bismuth is a non-magnetic, rather heavy metal ($Z = 83$) with semimetallic properties, i.e. the Fermi surface consists only of two tiny pockets, so that the density of states (DOS) at the Fermi level (E_F) is almost zero. In the surface projected bulk-bandstructure extended gaps are observed around E_F, in which surface states can be localized.

ARPES measurements on the Bi(110) surface [28] showed the existence of two spectroscopic features in the gap, which could be interpreted as to two surface states. Bismuth has a rhombohedral crystal structure and the (110) surface consists of unreconstructed pseudocubic bilayers [29], where dangling bonds can give rise to surface states. Similarly, on Bi(111) two states were identified spectroscopically [30]. The (111) surface has closed-packed layers and again shows a bilayer structure, but without dangling bonds and with a much larger separation of the bilayers [31]. In both cases of course only the occupied part of the surface bandstructure could be observed spectroscopically. Using DFT calculations, we have the possibility to access also the unoccupied part of the spectrum. It can be seen that the observed spectroscopic features are actually a Rashba-type spin-split pair of a surface state which forms – at least for the (110) and (100) surface – a band through the whole surface Brillouin zone [32, 33]. That these surface state is actually split by spin-orbit coupling can be demonstrated by comparison of a scalar-relativistic calculation without inclusion of SOC and with the inclusion of SOC [34] (cf. also left of figure 8). In this cases, the splittings are very large (in the order of 300 meV) and, since the surface states extend throughout the Brillouin zone, they are also no longer linear in k, except in the vicinity of high symmetry points.

It is not only of academic interest, whether two surface states are a spin-split pair or two spin-degenerate surface states. For example, on the Bi(111) surface the Fermi surface forms a small hexagon around the $\overline{\Gamma}$ point, which led to speculations about the formation of a charge density wave on this surface [35]. If the Fermi surface were indeed formed by spin-degenerate surface states, this would be possible. If, on the other hand, Rashba-type spin-split bands form this part of the Fermi surface, the electrons at $+\mathbf{k}_{\|}$ and $-\mathbf{k}_{\|}$ were of opposite spin and instead of a peak in the (spin) diagonal part of the susceptibility χ, we would expect a large contribution to the spin off-diagonal part, $\chi^{\pm}$, leading to a modulation of the spin-structure. Since the surface is of course still nonmagnetic, these modulations have to cancel and a direct observation is difficult. When magnetic atoms were present at the surface, their interaction would be modified and this effect could be detected. We will show in a later chapter, that this is actually possible.

Using scanning tunneling microscopy (STM) techniques, consequences of the spin polarization of the surface states have indeed been observed for another Bi surface [32]. If a scanning tunneling spectrum (STS) is recorded for a dense mesh of positions on a surface, this STS map can be Fourier transformed for a given energy within this spectrum. The Fourier transformed (FT) STS map gives then a picture of the energy dispersion in reciprocal space, i.e. a two dimensional cut through the function $\varepsilon(\mathbf{k}_{\|})$, but with doubled length of the $\mathbf{k}$-vectors, since the STS maps the scattering between two states of different $\mathbf{k}$ but at the same E. In particular, for $E = E_{\mathrm{F}}$, this yields an image the Fermi surface. It is easily seen, that a surface state with a Fermi surface of a wavevector $\pm\mathbf{k}_{\mathrm{F}}$ will give rise to standing waves with $2\mathbf{k}_{\mathrm{F}}$ which can be seen in the STS map. This correspondence between FT-STS and Fermi surface has been used extensively to study the electronic properties of high-temperature superconductors. A Rashba splitting will not change this picture, since for one spin channel the Fermi vectors are changed to $\pm\mathbf{k}_{\mathrm{F}} + \Delta\mathbf{k}$, while for the other spin we get $\pm\mathbf{k}_{\mathrm{F}} - \Delta\mathbf{k}$, so that both spin channels will lead to a contribution of $\pm 2\mathbf{k}_{\mathrm{F}}$ in the STS map, i.e. the picture is indistinguishable from the one without Rashba splitting [27]. But if the Fermi surface is more complex, like in the case of Bi(110), the fact, that the surface states are spin polarized can be seen the FT-STS clearly.

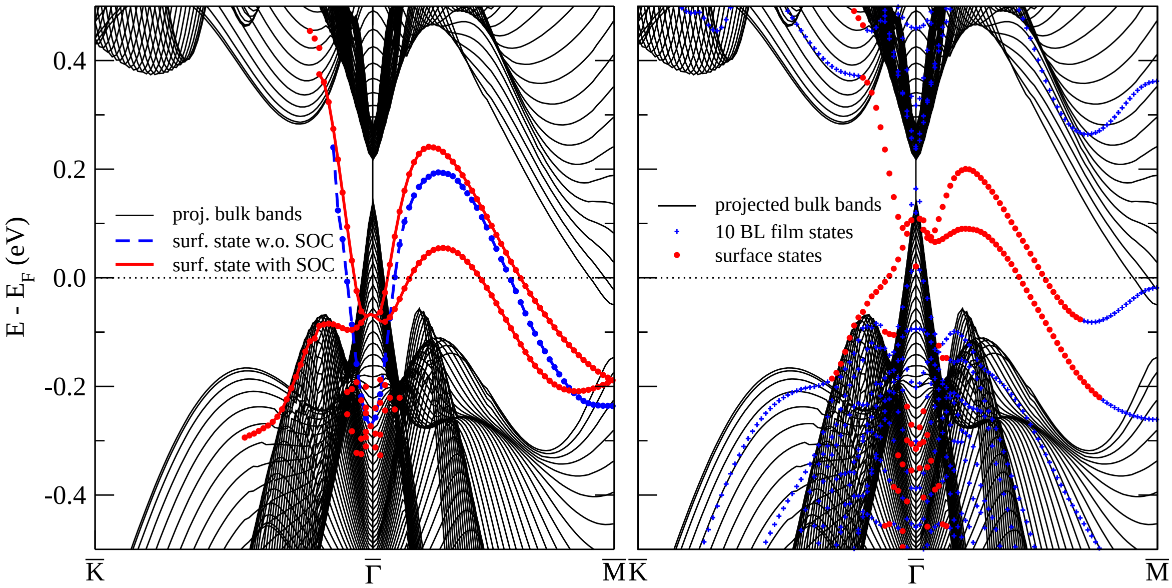

Figure 8: Bulk-projected bandstructure of Bi and surface bandstructure of a 22 layer Bi(111) film with H termination on one side (left) with (full line) and without (broken line) spin-orbit coupling included in the calculation. A similar calculation with SOC included for a symmetric 20 layer film without H termination is shown on the right.

Consider a simple one-dimensional example: along the line $\overline{\Gamma\mathrm{M}}$ in Bi(111) we can see in figure 8 (left, broken line) a surface state obtained without inclusion of SOC. This state originates at

-0.3 eV at $\overline{\Gamma}$, crosses the Fermi level at a wavevector we denote k_a, disperses down again and crosses $E_{\rm F}$ once more at k_b and reaches $\overline{\rm M}$ at -0.22 eV. Surface states at $E_{\rm F}$ can scatter between k_a and k_b and give rise to standing waves with wavelength $2k_a, 2k_b, (k_a + k_b)$ and $(k_a - k_b)$, if the state is spin-degenerate. Now, consider that spin-orbit coupling splits this degeneracy and gives rise to spin-up states at $k_a + \Delta k$ and $k_b - \Delta k$, while spin-down states cross the Fermi level at $k_a - \Delta k$ and $k_b + \Delta k$. In this case, spin conserving scattering events will again give rise to oscillations with wavelength $2k_a, 2k_b$, but also $(k_a + k_b) \pm 2\Delta k$ and $(k_a - k_b) \pm 2\Delta k$. Here, the effect of spin is clearly visible. On the Bi(110) surface, this effect was also verified experimentally in a two dimensional case [32].

The occurrence of spin-polarized surface states of course suggests, that this could be utilized in some way for spintronic applications. In the case of Ag(111), where the surface state contributes very little to the density of states at the Fermi level, this might not seem very promising, but in the case of a semimetal surface, where the DOS at $E_{\rm F}$ originates almost exclusively from surface states, this might be more realistic. Alternatively, the surface of a thin film on insulating or semiconducting substrates could be interesting, since in this case the relative contribution of the surface state to the conduction electrons is also increased. This works of course only, if the thin film still supports the same surface state as the semiinfinite crystal, i.e. localized Tamm states of d-character as they occur on lanthanide (0001) surfaces will be more suitable for very thin films than the extended s, p-derived Shockley states of the closed packed coinage metal surfaces.

Another effect, that can disturb the surface states in thin films, is the interaction between the two surfaces of the film. If, like in Bi, the screening is very weak, surface states at the upper and lower surface of a symmetric film interact to form even and odd linear combinations. This of course interferes with the concept of broken inversion symmetry at the surface. On the other hand, in our theoretical calculations for Au and Ag surfaces, we always used symmetrical films where a tiny interaction between upper and lower surface cannot be avoided, even in thicker films. For the bandstructures of figure 7 we used 23 layer films and especially in the case of Ag(111), a finite splitting of the surface state parabolas at the $\overline{\Gamma}$ point can be seen. At the first glance it might seem surprising, that the two different splittings, the even-odd and the Rashba-type splitting result in only two dispersion curves. Without the interactions that lead to the splittings, we can think of having two states (spin up, $\uparrow$ and down, $\downarrow$) on each surface. The spin-orbit coupling leads for the spin up states of the upper surface ($\uparrow_u$) to the same shift in energy as for the spin down states of the lower surface ($\downarrow_l$) (since the potential gradient is reversed there) and they will have an energy ε^+. In the same way of course $\varepsilon(\downarrow_u) = \varepsilon(\uparrow_d) = \varepsilon^-$. A hybridization of $\uparrow_u$ and $\downarrow_u$ leads to energies $\varepsilon^+ + \varepsilon^s$ and $\varepsilon^- - \varepsilon^s$, respectively, but in the same way the two downspin states, $\downarrow_u$ and $\downarrow_l$ will be shifted to energy values $\varepsilon^- - \varepsilon^s$ and $\varepsilon^+ + \varepsilon^s$. The stronger the interaction across the film, the more each state will be localized at both sides of the film so that finally the spin-polarization for a given energy and $\mathbf{k}_{||}$ gets reduced.

A case, where this scenario has been actually observed in experiment are thin Bi films grown on a Si substrate [36]. The interaction with the substrate is very weak, since the Bi film is deposited on a seeding layer of Bi atoms and can adopt (for more than a few bilayers) the structure of Bi(111). Angle resolved photoemission has shown that near the zone center the electronic structure of these Bi films is not so different from what has been observed on single crystal surfaces. But when the $\mathbf{k}_{||}$ vector approaches the zone boundary at $\overline{\rm M}$, the crossing of the two spin-split states is no longer observed. Instead, quantum well states (QWS) are formed when the surface state gets near to the bulk continuum at $\overline{\mathrm{M}}$ [36]. The energy levels of these states agree nicely with those obtained by the calculation of symmetric films of the same thickness (cf. right of figure 8). As the surface state character is lost, also the spin-polarization of these states vanishes. The very bad screening of Bi makes this QWS disappear only for very thick films (more than 40 bilayers). Therefore, when we simulate Bi single crystal surfaces, we have to terminate one side of the film with H atoms to saturate the dangling bonds and explicitly remove the inversion symmetry of the film, even if it is 22 layers thick.

2.3 Magnetic Surfaces

Let us finally consider the case of a surface of a magnetic metal, like Gd(0001). On this closed packed surface a bulk projected bandgap around $\overline{\Gamma}$ contains a surface state of d_{z^2} character, like it can be found also on other lanthanide surfaces. Exchange interaction splits this surface state into an occupied majority spin state and an unoccupied minority state. This splitting is mainly controlled by the $4f$ electrons of Gd and amounts to about 0.8 eV, which is large as compared to spin-orbit effects in this system. No matter how SOC affects the electrons of the surface state, their spin will remain more or less parallel to the exchange field, which is oriented in plane in the directions of nearest neighbor atoms by the magnetic anisotropy.

An electron traveling on the surface in a direction *perpendicular* to its spin quantization axis, will experience the potential gradient at the surface as a magnetic field parallel to its spin. Therefore, a magnetic coupling can arise and the dispersion curves will split more or less similar to what is observed on a nonmagnetic surface. If, on the other hand, the propagation direction of the electron is parallel to its spin quantization axis, the field arising from SOC cannot couple to the electron's spin and no Rashba-like splitting can be observed. Schematically, this situation is shown in figure 9. In contrast to the surface state on the nonmagnetic surface, where the spin of the electron is always oriented perpendicular to the propagation direction and the surface normal, $\mathbf{e}_z$, (with some deviation, depending on the shape of the potential [24]), on the spin-polarized surface, the spins are more or less collinear. This changes the shape of the Fermi surface significantly, especially if exchange splitting is considered (figure 9 (c)). If the exchange splitting is large, this leads to a Fermi surface consisting of a single circle shifted away from the zone center. The consequences for the bandstructure are simple: along a certain direction in reciprocal space SOC will have no particular effect. In a direction orthogonal to this one, the dispersion curves for majority and minority spin will be shifted in opposite directions. For the eigenvalues this results in an expression

$$\varepsilon_{\downarrow(\uparrow)}(\mathbf{k}) = \varepsilon(\mathbf{k}) \pm IM \pm \alpha_{\mathrm{R}}(\mathbf{k} \times \mathbf{e}_z) \cdot \hat{\mathbf{M}} \tag{16}$$

where $\mathbf{M} = M\hat{\mathbf{M}}$ is the magnetization and IM represents the exchange splitting of the bands. Of course in a calculation of a symmetric film, again on the lower surface ($-\mathbf{e}_z$) the directions of the spin-orbit induced shifts will be exactly opposite to the shifts on the upper surface, so that in total a picture as shown in figure 9 (d) is obtained. From this picture the two splittings for the spin-up and the spin-down surface state can be determined directly as $\Delta\varepsilon(\mathbf{k}) = \varepsilon(\mathbf{k}, \mathbf{M}) - \varepsilon(\mathbf{k}, -\mathbf{M})$.

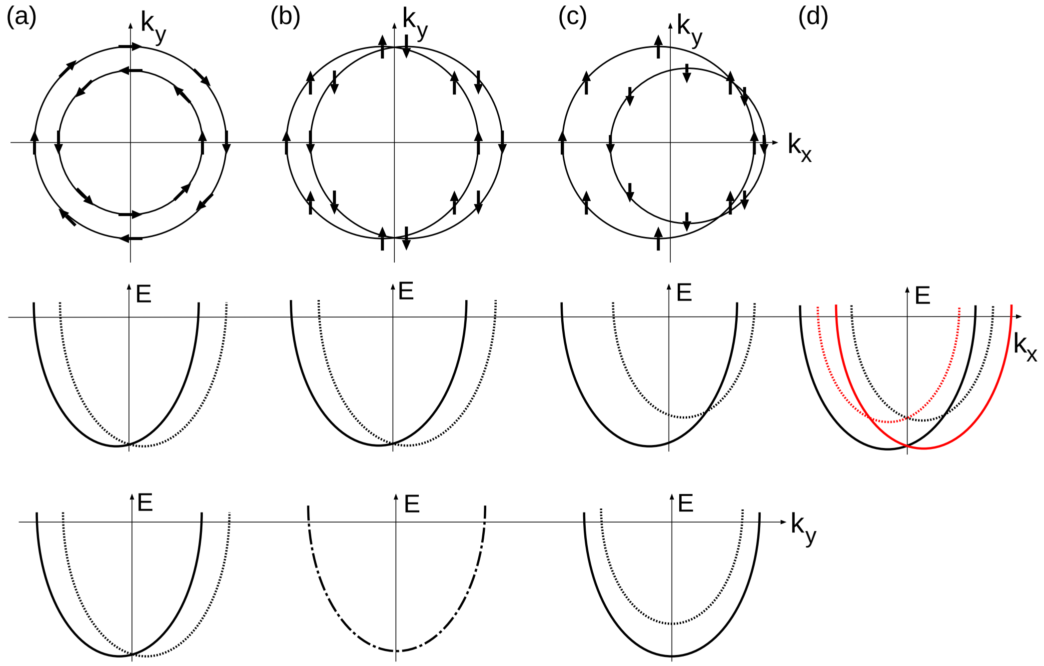

Figure 9: (a): Rashba splitting on a non-magnetic surface: the top panel shows the Fermi surface and the spin-polarization of the states at the Fermi level. In the middle and lower panel the bandstructures along two orthogonal directions in reciprocal space are shown. (b): The same relations as in (a) are shown, but now for the case where the spin-quantization axis of the electrons has been aligned in a particular direction. For electrons propagating in this direction, the Rashba splitting vanishes. (c): Effect of an additional exchange splitting on the situation as described in (b). (d): Surface bandstructure arising from the calculation of a symmetric film, where the surface states from the lower surface are shown in red.

Experimentally, for a single crystal surface, it is possible to measure with ARPES two spectra of the same surface, but rotated by 180 degrees. In the case of an in-plane anisotropy, as for Gd(0001), this rotation reverses the spin and leads, therefore, also to a picture as figure 9 (d). A comparison of these two spectra allowed to determine the Rashba splitting in Gd(0001), even though its magnitude is rather small [37]. A particular advantage of magnetic surfaces is, that the measurements allow the determination of the sign of the Rashba parameter, α_R, even without the need of spin-analysis via a Mott detector.

Modification of the Gd surface also alters the characteristics of the surface state: if (atomic) oxygen is adsorbed in the surface, the surface state shifts down in energy and both, minority and majority spin states become occupied. Moreover, the dispersion of the surface state changes from almost flat on Gd(0001) to parabolic for O/Gd(0001). Both surface states were observed experimentally, and DFT calculations show, that these states are actually interface states residing between the topmost Gd/O layer and the underlying Gd bulk [37].

Let us now focus on the Rashba-type splitting on O/Gd(0001). In figure 10 we plotted the splitting as a function of $k_{\|}$ for the directions $\overline{\Gamma \mathrm{M}_1}$ and $\overline{\Gamma \mathrm{K}_1}$ as indicated in the figure. Since the magnetization is directed towards nearest neighbours (a-direction), the largest effects on the surface state dispersion should be observed in $\overline{\Gamma \mathrm{M}_1}$ direction while no splitting should be

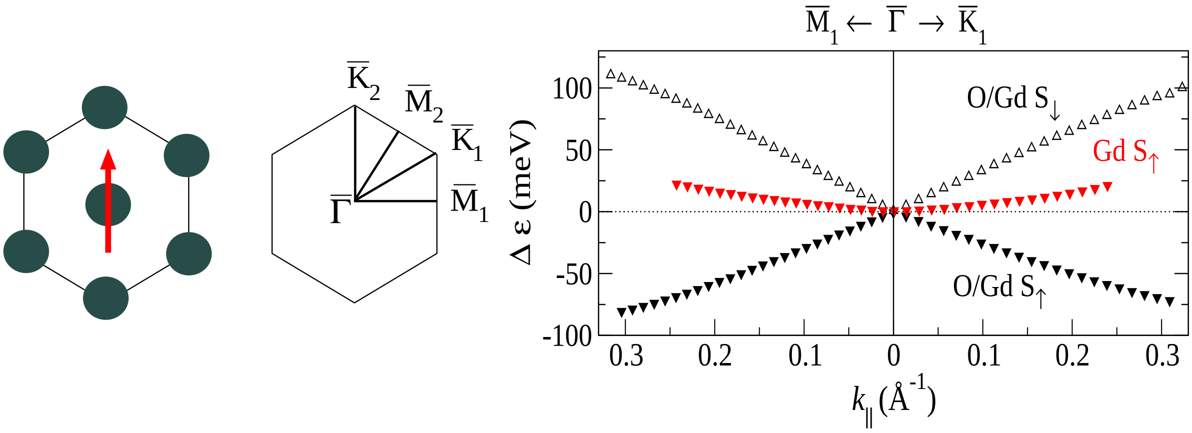

Figure 10: Left: Magnetization direction on the Gd(0001) surface indicated by the red arrow and surface Brillouin zone and labeling of the high symmetry points. Right: Rashba-type splitting of the surface state of Gd(0001) and O/Gd(0001) in the directions $\overline{\Gamma\mathrm{K}_1}$ and $\overline{\Gamma\mathrm{M}_1}$.

visible in the direction $\overline{\Gamma\mathrm{K}_2}$. A closer look at figure 10 reveals, that the splitting, $\Delta\varepsilon$ is indeed smaller in $\overline{\Gamma\mathrm{K}_1}$ than in $\overline{\Gamma\mathrm{M}_1}$. Furthermore, we observe that $\Delta\varepsilon$ for the majority spin state ($\mathrm{S}_\uparrow$) is not only of opposite sign as compared to $\Delta\varepsilon$ for the minority state ($\mathrm{S}_\downarrow$), but also their absolute values differ. This is also observed experimentally, and can be explained again by the different positions of the states in the bulk-projected bandgap and the different asymmetry of the wavefunctions. One should note here, that also the effective masses of the $\mathrm{S}_\uparrow$ and $\mathrm{S}_\downarrow$ states differ and this shows, that spin is not the only difference of these states.

Even more drastic is the difference of the $\mathrm{S}_\uparrow$ surface state of O/Gd(0001) to the $\mathrm{S}_\uparrow$ state of Gd(0001). We can see from the right of figure 10 that not only the magnitude of the splitting is a factor 3 to 4 smaller, even the sign is different. Since this reversal of sign cannot be attributed to the spin, it must result from a different admixture of p_z-character to the d_{z^2} surface state. A reversal of the gradient of the wavefunction at the position of the Gd nucleus can be interpreted as the result of hybridization with p_z-type wavefunctions of different signs. In some sense we can say, that we see the sign of the wavefunction here in the sign of the Rashba-parameter.

3 Anisotropic exchange of adatoms on surfaces

In the last subsection, we assumed that the magnetic order at the surface is not influenced by spin-orbit coupling effects. If the exchange field is strong, all spins will align accordingly. On the other hand, if the exchange coupling is weak, spin-orbit coupling effects can substantially influence the magnetic interaction. The particular case of two distant impurities, which interact in a RKKY-type manner via a non-magnetic host which shows strong spin-orbit effects has been discussed by Smith [38]. He showed that the interaction between two magnetic atoms A and B (spins $\mathbf{S}_A$ and $\mathbf{S}_B$) via a non-magnetic third atom with a SOC term $\mathbf{l} \cdot \mathbf{s}$ gives rise to an interaction $(\mathbf{S}_A \cdot \mathbf{s})(\mathbf{l} \cdot \mathbf{s})(\mathbf{s} \cdot \mathbf{S}_B)$. Taking the trace over the spin variable $\mathbf{s}$ this term can be written as $(-i/4)\mathbf{l} \cdot (\mathbf{S}_A \times \mathbf{S}_B)$ and thus shows the form of the Dzyaloshinskii-Moriya (DM) interaction $\mathbf{D}\cdot(\mathbf{S}_A\times\mathbf{S}_B)$. Fert and Levy [39] derived an expression for this anisotropic exchange interaction of two magnetic atoms in spin-glasses doped with heavy impurity atoms which is of the form

$$H_{\mathrm{DM}} = -V(\xi)\frac{\sin\left[k_{\mathrm{F}}(R_A+R_B+R_{AB})+\eta\right]\hat{\mathbf{R}}_A\cdot\hat{\mathbf{R}}_B}{R_A R_B R_{AB}}(\hat{\mathbf{R}}_A\times\hat{\mathbf{R}}_B)(\mathbf{S}_A\times\mathbf{S}_B) \tag{17}$$

where $\mathbf{R}_A = R_A\hat{\mathbf{R}}_A$ and $\mathbf{R}_B = R_B\hat{\mathbf{R}}_B$ are the positions of the magnetic atoms measured from the nonmagnetic impurity and R_{AB} is the distance between the atoms A and B. $V(\xi)$ is a term that depends of the spin-orbit coupling constant of the nonmagnetic atom, ξ, k_{F} is the Fermi vector and η the phase shift induced by the impurity. The sinus term reflects the RKKY-type character of the interaction, while the two cross products determine the symmetry of the interaction.

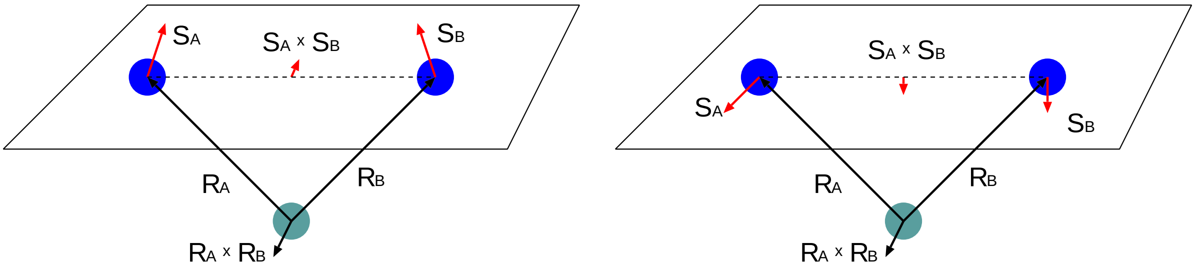

Figure 11: Two magnetic adatoms (A, B) on a surface interacting with a surface atom at the center. The distance between the surface atoms and the adatoms is $\mathbf{R}_A$ and $\mathbf{R}_B$. The spins of the adatoms are almost perpendicular to the surface (left) or in the surface plane (right), but sightly canted to give a finite value for $\mathbf{S}_A\times\mathbf{S}_B$

This model can be translated to the case of two magnetic atoms on a surface, where the magnetic interaction is mediated by surface states which show strong SOC effects. Such a situation might be imagined, if e.g. two Mn atoms are placed on a Bi surface (figure 11). If the easy magnetic axis is out-of-plane, a slight tilting of the magnetic moments results in a finite value for $\mathbf{S}_A\times\mathbf{S}_B$ which is then parallel to $\hat{\mathbf{R}}_A\times\hat{\mathbf{R}}_B$ and leads to a non-vanishing contribution of H_{DM} (equation (17)). If the easy magnetic axis is in-plane (right of figure 11) and the surface normal is the hard axis, a small tilting of the magnetic moments results in a vector $\mathbf{S}_A\times\mathbf{S}_B$ that is normal to $\hat{\mathbf{R}}_A\times\hat{\mathbf{R}}_B$ and equation (17) will give no contribution to the total energy. Of course, on a surface the scattering will involve all surface atoms and in general it will depend not only on the direction of the spins of the adatoms, but also on the symmetry of the surface whether a DM interaction will occur for a specific arrangement of the spins. This will be discussed later in more detail.

If we extend the two impurities in figure 11 to a chain of magnetic atoms, where the spins of two neighbouring atoms, i and j, are canted slightly, an interaction of this kind

$$H_{DM} = \mathbf{D}_{ij}\cdot(\mathbf{S}_i\times\mathbf{S}_j) \tag{18}$$

will favour spin-spiral structure. Since the DM interaction has to compete with the Heisenberg-type (symmetric) exchange interaction, these structures will probably be of long wavelength. Such long-ranged magnetic structures can be found on surfaces in domain walls of thin magnetic films. In the following we will discuss the consequences of the DM interaction on this kind of long ranged, non collinear structures, and show results of *ab initio* calculations for a system that has also been investigated experimentally in some detail.

4 Mesoscale magnetic structures

In this section, we discuss magnetic structures on the mesoscopic length scale that are driven by the DM interaction. Since the DM interaction is a purely relativistic effect, we expect it to be much weaker than the usual exchange interactions. In most cases, it cannot cause more than a small canting angle between the spins on adjacent lattice sites, and the local magnetic structure (typically ferro- or antiferromagnetic) is governed by non-relativistic effects. For spatially slowly varying magnetic structures, however, the DM interaction can become relevant since it is antisymmetric whereas the non-relativistic exchange interactions are all symmetric with respect to the canting angle. The symmetric interactions lack any linear terms in the usual Taylor expansions in the canting angle, whereas an antisymmetric interaction shows such a term. In the following, we employ a simple model in order to describe the mesoscale magnetic structures that can arise from an interplay of spin stiffness, usual anisotropy and the Dzyaloshinskii-Moriya interaction. It is not the aim of this section to give a complete overview of the possible magnetic structures arising from the DM interaction at surfaces, but our simple model already illustrates the variety of possible magnetic structures.

4.1 Micromagnetic model

We restrict our further investigations to a quasi one-dimensional model where the magnetization depends on only one spatial coordinate x, and we denote the corresponding real-space direction as propagation direction (cf. figure 12). The quasi one-dimensional model is justified for anisotropic crystal structures where the magnetization is expected to propagate along a high-symmetry line and for simple domain walls where the magnetization is expected to propagate normal to the real-space orientation of the domain boundary. But our ansatz cannot describe vortices and other mesoscale magnetic structures that are well discussed in literature (cf. e.g. [40]).

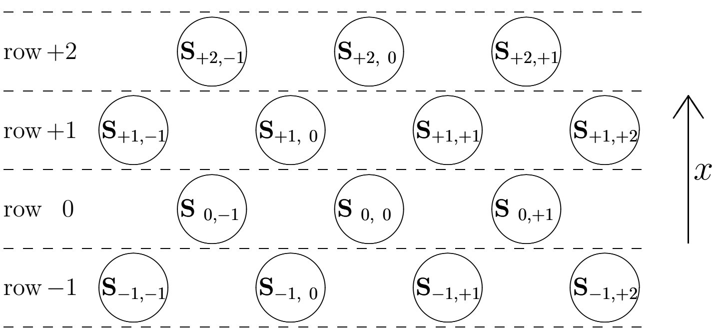

Figure 12: Atomic rows. In the quasi one-dimensional model, we assume that the magnetization direction changes along the x-direction but remains constant within a row normal to the x-direction (i.e. $\mathbf{S}_{j,i} = \mathbf{S}_{j,i'}$). The x-direction is called propagation direction.

As we want to investigate magnetic structures, that change on length scales that are large compared to the lattice spacing, we can employ a micromagnetic model. In such a model, the magnetization direction is not described by a discrete set of unit vectors $\{\mathbf{S}_j\}$ but by a continuous function $\mathbf{m}(x)$ with $|\mathbf{m}| = 1$. This ansatz works for ferromagnetic and antiferromagnetic materials alike: In the case of an antiferromagnetic structure, $\mathbf{m}(x)$ is oriented parallel and antiparallel respectively to every second atomic moment $\mathbf{S}_j$.

If all relevant interactions are reasonably short-ranged, we can estimate the energy of a magnetic configuration (in a homogeneous crystal) by

$$E[\mathbf{m}] = \int \mathrm{d}x \, f(\mathbf{m}, \dot{\mathbf{m}}) \tag{19}$$

with $\dot{\mathbf{m}}(x) = \frac{\mathrm{d}}{\mathrm{d}\,x}\mathbf{m}(x)$. The structure of the function f can be deduced from a discrete lattice model, for instance the classical Heisenberg model $\sum_{i,j} J_{i,j}\, \mathbf{S}_i \cdot \mathbf{S}_j$ corresponds to a term of the form $\int \mathrm{d}x\, A\, \dot{\mathbf{m}}(x)^2$ (cf. e.g. [41]). But the integrand $A\, \dot{\mathbf{m}}(x)^2$ can also be regarded as the lowest order Taylor expansion to an arbitrary symmetric $\dot{\mathbf{m}}$-dependent function. Thus, the parameter A includes all non-relativistic exchange effects in the limit of spatially slowly varying magnetic structures, even if the system is badly described by the Heisenberg model.

In the following, we consider a term symmetric in $\dot{\mathbf{m}}$ (that prevents spin rotations on short length scales), a term antisymmetric in $\dot{\mathbf{m}}$ (that favors certain spin rotations), and the lowest order anisotropy term and we work with the energy functional

$$E[\mathbf{m}] = \int \mathrm{d}x \, \Big(A\, \dot{\mathbf{m}}(x)^2 + \mathbf{D} \cdot (\, \mathbf{m}(x) \times \dot{\mathbf{m}}(x)\,) + \mathbf{m}(x)^{\dagger} \cdot \mathsf{K} \cdot \mathbf{m}(x)) \Big) \; . \tag{20}$$

The model parameters are the spin stiffness A, the Dzyaloshinskii vector $\mathbf{D}$ and the anisotropy tensor K. As we assume, that the magnetization propagates along a high symmetry line of a rectangular surface, we know the direction of the Dzyaloshinskii vector $\mathbf{D}$ and the structure of the anisotropy tensor K: $\mathbf{D}$ is oriented perpendicular to the x-direction and perpendicular to the surface normal (cf. figure 13), and K is diagonal if we choose our coordinate axis along the high symmetry directions of the crystal. With such a coordinate system, we get:

$$\mathbf{D} = \begin{pmatrix} 0 \\ 0 \\ D \end{pmatrix} \quad , \quad \mathsf{K} = \begin{pmatrix} K_1 & 0 & 0 \\ 0 & K_2 & 0 \\ 0 & 0 & K_D \end{pmatrix} \; . \tag{21}$$

4.2 Planar spin structures

From equation (20) it is obvious, that the DM term is minimized if the magnetization rotates in the plane normal to the Dzyaloshinskii vector $\mathbf{D}$. If the hard axis is oriented parallel to $\mathbf{D}$ (i.e. $K_D > K_1$, $K_D > K_2$), then the anisotropy term also favors a magnetization that is confined to the plane normal to $\mathbf{D}$. At first, we restrict our considerations to this case. In such a system with $\mathbf{m} \perp \mathbf{D}$, we can describe the magnetization with only one angle φ ($\mathbf{m} = \hat{\mathbf{e}}_1 \cos\varphi + \hat{\mathbf{e}}_2 \sin\varphi$) and obtain the energy functional

$$E[\varphi] = \int \mathrm{d}x \, \big(A\, \dot{\varphi}(x)^2 + D\, \dot{\varphi}(x) + K \sin^2 \varphi(x) + \mathrm{const}\, \big) \tag{22}$$

with $K = K_2 - K_1$. Without loss of generality, we assume $K > 0$. The functional (22) is well discussed by Dzyaloshinskii. In the following we briefly state some of his results, for further details and analytical derivations cf. [42, 43].

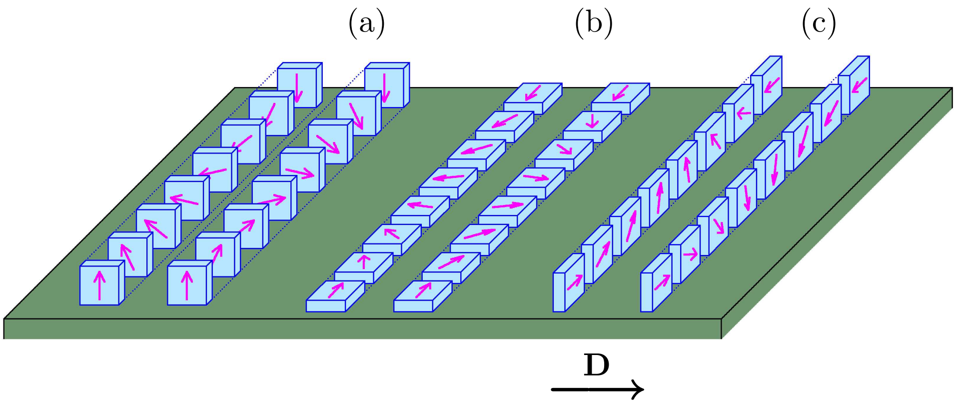

Figure 13: Spin spirals with different rotation axes on a symmetric surface. For each rotation axis, a right- and a left-handed spiral is shown. If we neglect the substrate, the right- and left-handed spirals are mirror images of each other. If we take spin-orbit coupling into account, we need to consider the system consisting of spiral and substrate. For (a) and (b), the mirror plane is oriented normal to the surface, therefore the surface does not break the mirror symmetry (provided that the spirals propagate along a high-symmetry line of the crystal structure). In the case (c), however, the surface breaks the mirror symmetry and there is no other symmetry operation mapping the right- onto the left-handed system. Therefore, the two systems in (c) are not equivalent to each other and may differ in energy. With equation (18), we conclude that **D** is orthogonal to the rotation axes of (a) and (b). Of course, the sign of **D** cannot be deduced from the symmetry.

If we neglect the anisotropy term $K\,\sin^2\varphi$, we obtain spin rotations for all non-vanishing D. But, for sufficiently large K the DM term cannot compete with the other terms and the energy is minimized by a collinear magnetization that is oriented along the easy axis (i.e. $\varphi(x) = 0 = \text{const}\,$). The model (22) shows a rotating spin structure as the ground state, if and only if

$$|D| > \frac{4}{\pi}\sqrt{A\,K} \quad\Leftrightarrow\quad |\tilde{D}| = \frac{|D|}{\sqrt{A\,K}} > \frac{4}{\pi}\;. \tag{23}$$

At the transition to the collinear ground state, the spiral's spatial period length λ diverges (cf. figure 14). This transition can be interpreted as a second-order phase transition with order parameter $1/\lambda$ and a kink in $\mathrm{d}E/\mathrm{d}\tilde{D}$.

If the DM term is not strong enough to cause a rotating spin structure, a ferromagnetic sample of sufficient size usually consists of several domains that posses different spin quantization axes. In this case, we can use equation (22) with the boundary conditions

$$\varphi(x) \xrightarrow{x\searrow-\infty} \pi \qquad , \qquad \varphi(x) \xrightarrow{x\nearrow+\infty} 0 \tag{24}$$

in order to describe a wall between two oppositely magnetized domains. Thereby, the size of the DM term cannot influence the domain-wall shape $\varphi(x)$ but alters the wall energy E:

$$E = \int_{-\infty}^{+\infty}\mathrm{d}x\,\left(A\,\dot{\varphi}^2 + K\,\sin^2\varphi\right) + \int_{-\infty}^{+\infty}\mathrm{d}x\,D\,\dot{\varphi} \qquad\text{with}\qquad \int_{-\infty}^{+\infty}\mathrm{d}x\,D\,\dot{\varphi} = \int_{\pi}^{\pi\pm\pi}\mathrm{d}\varphi\,D = D\,(\pm\,\pi)\;. \tag{25}$$

Minimizing the (A,K)-dependent term in equation (25) yields two degenerate solutions of opposite rotational directions, i.e. with opposite sign of $\dot{\varphi}(x)$. The D-dependent term is independent

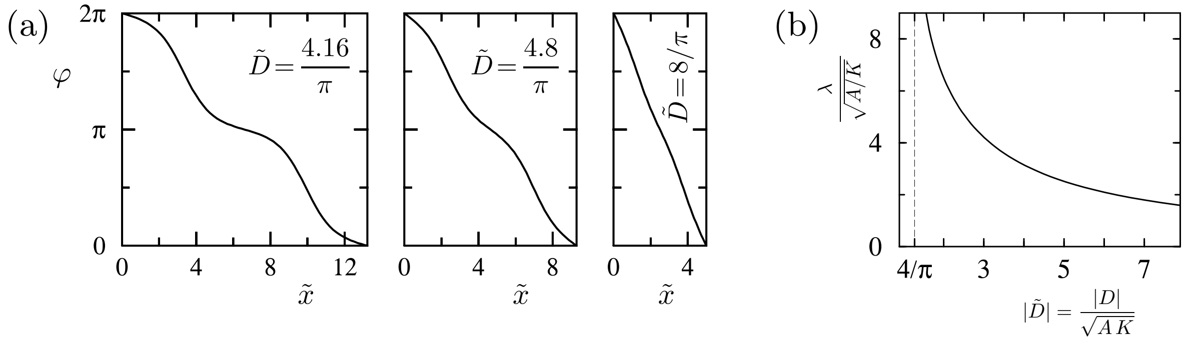

Figure 14: Influence of the model parameters on the ground state of equation (22). The model is characterized by one dimensionless parameter $\tilde{D} = \frac{D}{\sqrt{A\,K}}$. We use the reduced length $\tilde{x} = \sqrt{K/A}\,x$. (a): Magnetization direction of the periodically rotating ground state. For $\tilde{D} \searrow \frac{4}{\pi}$, the period length diverges and two collinear domains with $\sin^2\varphi = 0$ evolve. For $\tilde{D} < -\frac{4}{\pi}$, the rotational direction is reversed (i.e. $\dot{\varphi}$ changes sign). (b): Spatial period length λ with respect to the model parameters.

of the actual shape of $\varphi(x)$, but its sign depends on the rotational direction. It favors domain walls with $\operatorname{sign}\dot{\varphi} = -\operatorname{sign} D$. The functional $\int_{-\infty}^{+\infty}\mathrm{d}x\,\big(A\,\dot{\varphi}^2 + K\,\sin^2\varphi\big)$ with the boundary conditions (24) is minimized by the domain-wall shape $\varphi(x) = \arccos\,\tanh(\pm\sqrt{K/A}\,x)$ with the energy $4\sqrt{A\,K}$ [44]. Thus, from equation (25) we obtain an optimal domain-wall energy of

$$E = 4\sqrt{A\,K} - \pi\,|D|\;. \tag{26}$$

A negative domain-wall energy indicates, that the the system can gain energy by deviating from the collinear state. Therefore, $E = 0$ in equation (26) corresponds to the condition (23).

4.3 Three-dimensional spin structures

Of course, the assumptions made in equation (22) do not hold for all systems. In the following we still restrict our ansatz to the functional (20) and a crystal structure compatible with the definitions (21), but we do not impose any conditions to the anisotropy constants K_1, K_2, K_D. As a consequence, the magnetization vector $\mathbf{m}$ is not necessarily confined to a single plane but can rotate on a three-dimensional path in spin space. Although we still work with only one spatial coordinate, our model already illustrates the variety of magnetic structures that can arise from an interplay of spin stiffness and spin-orbit-coupling effects in anisotropic crystals.

Our model can be described with two dimensionless parameters $\tilde{D}$ and $\tilde{K}$. For $K_2 \neq K_1$ we can define

$$\tilde{D} = \frac{D}{\sqrt{A\,|K_2 - K_1|}} \quad , \quad \tilde{K} = \frac{K_D - K_1}{|K_2 - K_1|} \quad , \quad \tilde{x} = \sqrt{\frac{|K_2 - K_1|}{A}}\,x \quad , \quad \tilde{E} = \sqrt{\frac{1}{A\,|K_2 - K_1|}}\,E \tag{27}$$

and consider the functional

$$\tilde{E} = \int \mathrm{d}\tilde{x}\,\Big(\dot{\vartheta}^2 + \sin^2\vartheta\,(\,\dot{\varphi}^2 + \tilde{D}\,\dot{\varphi} + \sin^2\varphi - \tilde{K}\,)\Big) \tag{28}$$

with the $\tilde{x}$-dependent angles defined by $\mathbf{m} = \hat{\mathbf{e}}_1\,\sin\vartheta\,\cos\varphi + \hat{\mathbf{e}}_2\,\sin\vartheta\,\sin\varphi + \hat{\mathbf{e}}_D\,\cos\vartheta$. In the following, we present results that are obtained from a numerical analysis of the functional (28) [45, 46].

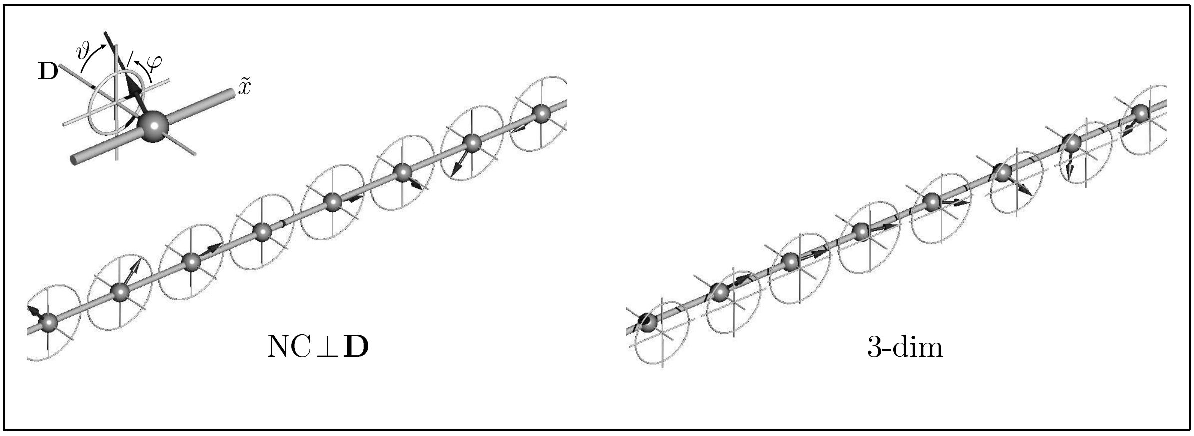

Figure 15: Noncollinear ground state of the functional (28). The left picture shows a planar rotating state ($\vartheta = \pi/2$) that occurs for large $|\tilde{D}|$, the right picture shows the state that occurs for intermediate values of $|\tilde{D}|$. The latter performs a truly three-dimensional path in spin space with $\vartheta \neq \text{const}$. Note, that $\mathbf{m}$ tries to avoid the hard axis that is oriented vertically in this figure.

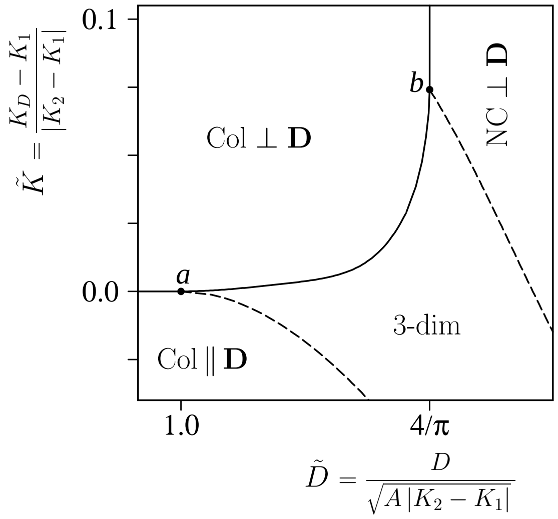

Figure 16: Phase diagram of the ground state of the functional (28). The diagram shows the collinear phase with $\mathbf{m}$ aligned perpendicular (Col $\perp$ $\mathbf{D}$) or parallel (Col $\|$ $\mathbf{D}$) to $\mathbf{D}$, the noncollinear (rotating) phase where $\mathbf{m}$ is confined to a plane (NC $\perp$ $\mathbf{D}$) and the noncollinear phase where $\mathbf{m}$ describes a truly three-dimensional path in spin spin space (3-dim). For $\tilde{D} < 0$ equivalent noncollinear phases occur with reversed rotational direction. The solid line denotes a first-order and the dashed lines denote continuous transitions. The two dashed lines approach each other for increasing $(-\tilde{K})$. For $K_1 = K_2$ the intermediate region (3-dim) vanishes and there is a sharp transition from the collinear state (Col $\|$ $\mathbf{D}$) to the planar rotating state (NC $\perp$ $\mathbf{D}$). Due to our choice of the reduced parameters (equation (27)), this transition point cannot be displayed in this figure.

For small $|\tilde{D}|$, the anisotropy term dominates the DM term and the ground state is collinear ($\vartheta = 0 = \text{const}$), for large $|\tilde{D}|$ the system is dominated by the competition between the DM interaction and the spin stiffness and the rotating magnetization is confined to the plane normal to the Dzyaloshinskii vector ($\vartheta = \frac{1}{2}\pi = \text{const}$, left picture in figure 15). If $\mathbf{D}$ points parallel to the easy axis (i.e. $\tilde{K} < 0$), there is a continuous transition from the collinear to the planar rotating ground state: When $|\tilde{D}|$ exceeds a certain critical value, then the magnetization starts to rotate around the $\mathbf{D}$-vector (i.e. $\operatorname{sign}\dot{\varphi} = -\operatorname{sign}\tilde{D} = \text{const}$), and the average cone angle ϑ increases with increasing $|\tilde{D}|$ (right picture in figure 15). If $\mathbf{D}$ does not point parallel to the easy axis, there is no continuous transition from the collinear to a rotating ground state possible: In this case a rotation around the $\mathbf{D}$-vector cannot be realized by an infinitesimal deviation from the collinear state. In figure 15 we illustrate the rotation path $\mathbf{m}(\tilde{x})$ of the ground state, in figure 16 we show the resulting phase diagram.

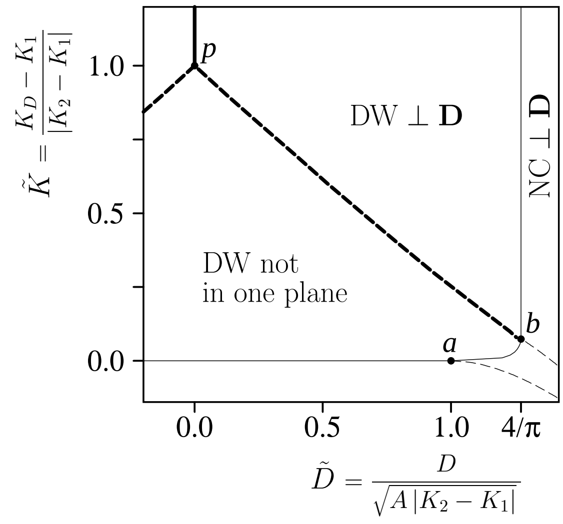

Figure 17: Phase diagram of the domain walls that are described by the functional (28). The thin lines show the transitions of the unconstrained structures (cf. figure 16), the bold lines indicate additional transitions of the domain-wall structures. For $\tilde{K} > 0$ the $\mathbf{D}$-vector points parallel to the hard axis. This case is already discussed in section 4.2. The solid line starting at p denotes the first-order transition that occurs when the preferable rotational direction reverses ($\operatorname{sign}\dot{\varphi} = -\operatorname{sign}\tilde{D}$). The dashed line from p to b denotes a second-order transition between wall structures with $\mathbf{m}(\tilde{x})$ confined to one plane (DW $\perp$ $\mathbf{D}$) and wall structures with $\mathbf{m}(\tilde{x})$ describing a three-dimensional path in spin space. Note, that the latter can exist also in the case of collinear aligned domain magnetization. The possible domain wall structures are further explained in the caption of figure 18.

Next, we turn our attention to the domain walls that can be described with our ansatz. We minimize the functional (28) under the boundary conditions

$$\tilde{x} \gg 1 \Rightarrow \begin{cases} \hat{\mathbf{e}}_{\text{easy}} \cdot \mathbf{m}(+\tilde{x}) > 0 \\ \hat{\mathbf{e}}_{\text{easy}} \cdot \mathbf{m}(-\tilde{x}) < 0 \end{cases} \tag{29}$$

where $\hat{\mathbf{e}}_{\text{easy}}$ denotes the unit vector that points parallel to the easy axis. This condition can be applied for the the collinear domains as well as for the three-dimensional ground states that are discussed above (cf. figure 15). A numerical investigation of the expressions (28) and (29) in the $(\tilde{K}, \tilde{D})$ parameter-space shows a variety of domain wall structures that can be classified in several distinct phases. The main results are summarized in the figures 17 and 18.

Figure 18: Rotation paths of $\mathbf{m}(\tilde{x})$ in the walls between collinear domains. In figures a-c the **D**-vector is perpendicular to the easy axis (i.e. $\tilde{K} > 0$), in figure d it is parallel to the easy axis (i.e. $\tilde{K} < 0$). (a): For $\tilde{D} = 0$ and $0 < \tilde{K} < 1$ there are two degenerate rotation paths in the plane normal to the hard axis. (b): For small $\tilde{D} > 0$ and $0 < \tilde{K} < 1$ the competition between the anisotropy term and the DM term results in a three-dimensional rotation path in spin space (in this figure, the hard axis is oriented vertically). There are still two degenerate solutions. (c): For larger $\tilde{D}$ or $\tilde{K} > 1$ the magnetization is confined to the plane normal to **D**. In this case, there is only one solution: the continuations of both walls in figure b coincide in the regime of $\mathbf{m} \perp \mathbf{D}$. (d): For **D** parallel to the easy axis, the domain walls reduce their energy by a spatial rotation around **D**.

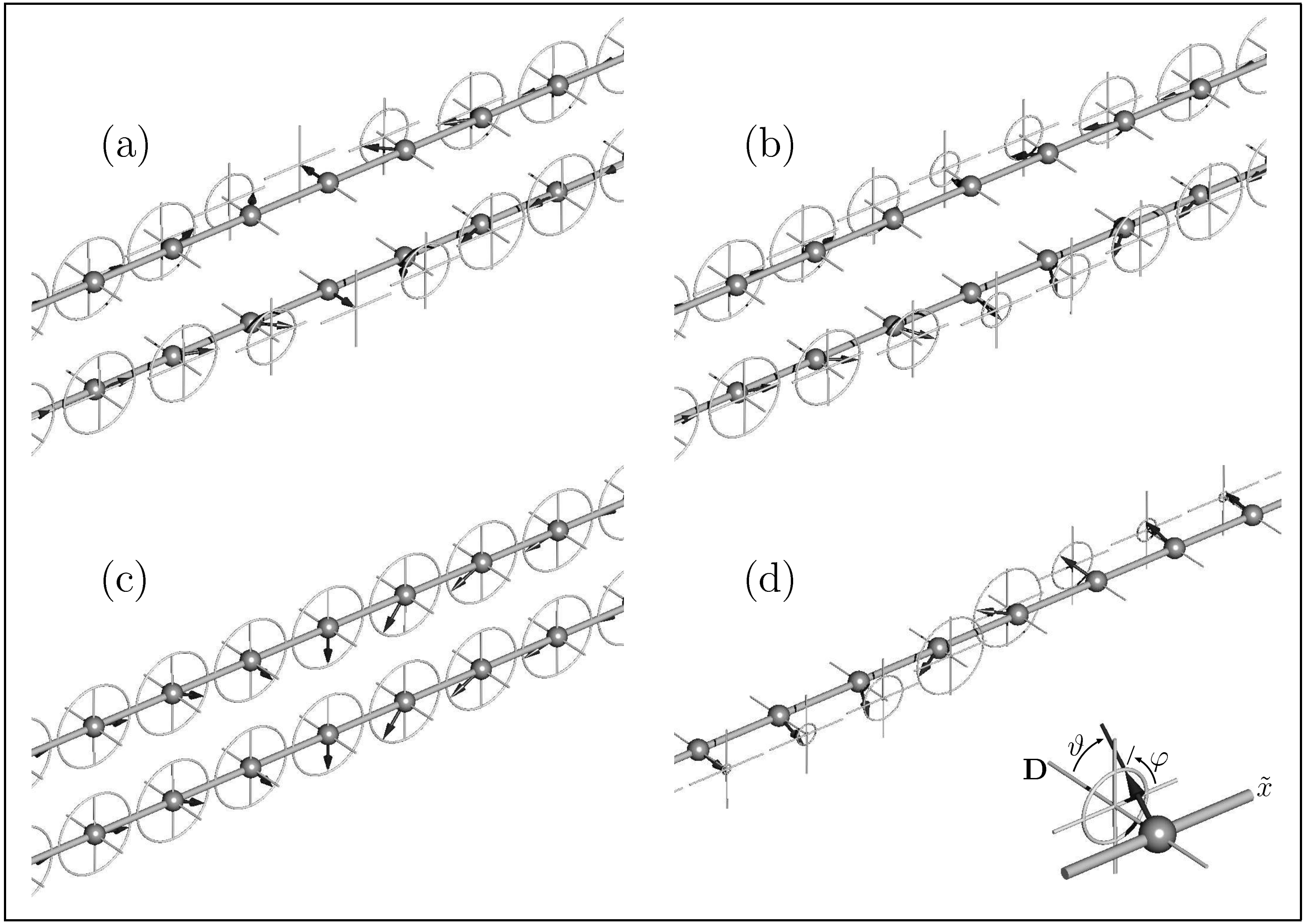

5 Dzyaloshinskii-Moriya interaction from first principles

5.1 DM-interaction within Multiple-Scattering Theory

Within multiple-scattering theory (MST) the DM constants $\mathbf{D}_{ij}$ can be found in an elegant way, as outlined in [47] and more recently in [48]. One employs the so-called "method of infinitesimal rotations", which provides the energy cost of an infinitesimal rotation of two spins, at sites i and j, within second-order perturbation theory. An underlying assumption is that the associated energy is related to the change of the single-particle energy levels only, i.e., one assumes again the validity of the magnetic force theorem. The change in the single-particle levels is then calculated in a straightforward way by utilizing Lloyd's formula, in a way analogous to the derivation of the Lichtenstein formula [10] for the Heisenberg exchange constants. Here, we follow the derivation by Udvardi et al. [48]. It is implied that the spin-orbit coupling is already included in the calculations of the electronic structure, scattering t-matrices, etc., before applying perturbation theory for the infinitesimal rotations.

We distinguish between two models for the description of the solid, which we will then bring in connection: (i) the density-functional model, including the charge and spin density $\rho(\mathbf{r});\mathbf{m}(\mathbf{r})$ at each point as a degree of freedom, and giving rise to a free energy $F[\mathbf{m};\rho]$; and (ii) an extended, classical Heisenberg-like model with a Hamiltonian $H(\mathbf{S}_i)$, including spin-spin interactions up to second order, and containing the directions of the magnetic moments at each atom, $\mathbf{S}_i$, as degrees of freedom. It is assumed that, for the system properties in question, a mapping of the free energy F of model (i) to the Hamiltonian H of model (ii) is meaningful. Such a mapping leads obviously to a significant reduction of the degrees of freedom to the essential ones for the problem at hand.

The spin-spin interaction can be described, up to second order, by the Hamiltonian

$$H = \sum_i K(\mathbf{S}_i) + \sum_{ij(i\neq j)} \mathbf{S}_i \mathsf{J}_{ij} \mathbf{S}_j \tag{30}$$

Here, the first term describes the on-site anisotropy energy and the second term (where $i \neq j$) includes the intersite exchange interactions and the Dzyaloshinskii-Moriya interaction. The quantities J_{ij} are 3×3 matrices (second rank tensors in real space). They can be decomposed in symmetric and antisymmetric parts as:

$$\mathsf{J}_{ij} = J_{ij}1 + \mathsf{J}_{ij}^S + \mathsf{J}_{ij}^A \tag{31}$$

with J_{ij} being the usual exchange interaction

$$J_{ij} = \frac{1}{3}\mathrm{Tr}\mathsf{J}_{ij}, \tag{32}$$

J_{ij}^S the (traceless) symmetric part

$$\mathsf{J}_{ij}^S = \frac{1}{2}\left(\mathsf{J}_{ij} + \mathsf{J}_{ij}^t\right) - J_{ij}1, \tag{33}$$

and J_{ij}^A the antisymmetric part:

$$\mathsf{J}_{ij}^A = \frac{1}{2}\left(\mathsf{J}_{ij} - \mathsf{J}_{ij}^t\right). \tag{34}$$

The latter can be brought in connection with the Dzyaloshinskii-Moriya interaction constants $\mathbf{D}_{ij} = (D^x_{ij}, D^y_{ij}, D^z_{ij})$ by writing

$$\mathsf{J}^A_{ij} = \left(\begin{array}{ccc} 0 & \frac{1}{2}(J^{xy}_{ij} - J^{yx}_{ij}) & \frac{1}{2}(J^{xz}_{ij} - J^{zx}_{ij}) \\ -\frac{1}{2}(J^{xy}_{ij} - J^{yx}_{ij}) & 0 & \frac{1}{2}(J^{yz}_{ij} - J^{zy}_{ij}) \\ -\frac{1}{2}(J^{xz}_{ij} - J^{zx}_{ij}) & -\frac{1}{2}(J^{yz}_{ij} - J^{zy}_{ij}) & 0 \end{array} \right) = \left(\begin{array}{ccc} 0 & D^z_{ij} & -D^y_{ij} \\ -D^z_{ij} & 0 & D^x_{ij} \\ D^y_{ij} & -D^x_{ij} & 0 \end{array} \right) \tag{35}$$

The spin-spin interaction is then written in terms of the Dzyaloshinskii-Moriya vectors as

$$\mathbf{S}_i \mathsf{J}_{ij} \mathbf{S}_j = J_{ij} \mathbf{S}_i \mathbf{S}_j + \mathbf{S}_i \mathsf{J}^S_{ij} \mathbf{S}_j + \mathbf{D}_{ij}(\mathbf{S}_i \times \mathbf{S}_j) \tag{36}$$

It is now necessary to express the interaction constants J^{xy}_{ij} etc. in terms of H; then the substitution $F \leftrightarrow H$ will make the connection to the density-functional model. We restrict the discussion to the off-diagonal elements, as these enter expression (35) for the Dzyaloshinskii-Moriya interaction. Evidently,

$$J^{xy}_{ij} = \frac{\partial^2 H}{\partial x_i \partial y_j}, \tag{37}$$

and similar expressions hold for the other components. These can be rewritten in terms of spherical coordinates (θ_i, ϕ_i) (defining the direction of magnetization $\mathbf{S}_i$). To obtain, for example, the expression of J^{zy}_{ij} in terms of H, it is convenient to choose a reference system in which the magnetization of the ferromagnetic state is along the x-axis, as sketched in fig. 19. In this reference system we get from eq. (30):

$$J^{zy}_{ij} = -\left(\frac{\partial^2 H}{\partial \theta_i \partial \phi_j} \right)_{\substack{\theta_{i,j}=\frac{\pi}{2} \\ \phi_{i,j}=0}}, \quad J^{yz}_{ij} = -\left(\frac{\partial^2 H}{\partial \phi_i \partial \theta_j} \right)_{\substack{\theta_{i,j}=\frac{\pi}{2} \\ \phi_{i,j}=0}}, \tag{38}$$

By choosing the magnetization along the y-axis, J^{xz}_{ij} and J^{zx}_{ij} can be obtained as:

$$J^{zx}_{ij} = -\left(\frac{\partial^2 H}{\partial \theta_i \partial \phi_j} \right)_{\substack{\theta_{i,j}=\frac{\pi}{2} \\ \phi_{i,j}=\frac{\pi}{2}}}, \quad J^{xz}_{ij} = \left(-\frac{\partial^2 H}{\partial \phi_i \partial \theta_j} \right)_{\substack{\theta_{i,j}=\frac{\pi}{2} \\ \phi_{i,j}=\frac{\pi}{2}}}, \tag{39}$$

while the J^{xy}_{ij} and J^{yx}_{ij} are found by placing the magnetization along the z-axis and taking infinitesimal rotations in the x and y directions (thus we set $\theta = 0$ and $\phi = 0, \frac{\pi}{2}$):

$$J^{xy}_{ij} = \left(\frac{\partial^2 H}{\partial \theta_i \partial \theta_j} \right)_{\substack{\theta_{i,j}=0 \\ \phi_i=0 \\ \phi_j=\frac{\pi}{2}}}, \; J^{yx}_{ij} = \left(\frac{\partial^2 H}{\partial \theta_i \partial \theta_j} \right)_{\substack{\theta_{i,j}=0 \\ \phi_i=\frac{\pi}{2} \\ \phi_j=0}}. \tag{40}$$

We now turn to the expressions of the change of free energy with respect to infinitesimal rotations of the magnetic moments within DFT, as derived by multiple-scattering theory. Again we follow the derivation by Udvardi et al. [48]. The contribution of the single-particle levels to the free energy at zero temperature is given in terms of the density of states $n(E)$, or the integrated density of states $N(E) = \int^E n(E')dE'$, as an integral up to the Fermi level E_F:

$$F = \int^{E_F} (E - E_F) n(E) dE = -\int^{E_F} N(E) dE. \tag{41}$$

By virtue of the magnetic force theorem, changes in the magnetization direction affect, to lowest order, only this single-particle part of the free energy. Therefore, the change in total energy can be directly associated with the changes in the integrated density of states.

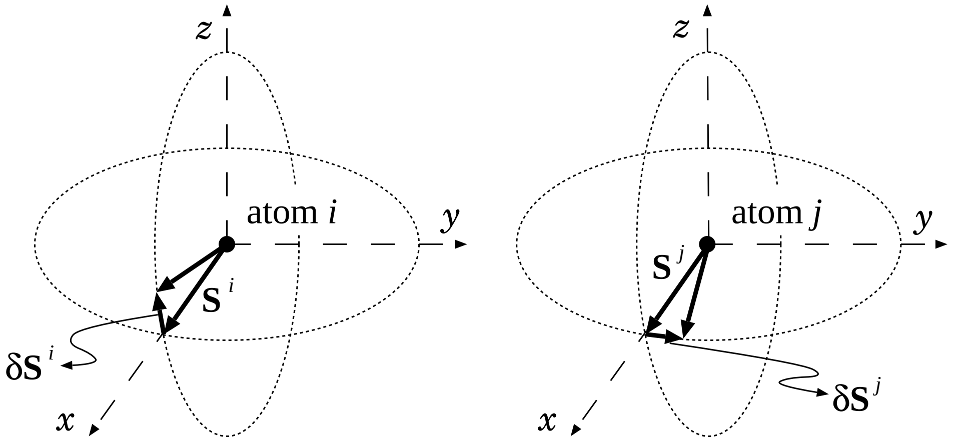

Figure 19: Setup for the calculation of the Dzyaloshinskii-Moriya interaction constants $\mathbf{D}_{ij}$. The magnetic moments of atoms i and j are tilted in different directions. Here, $\mathbf{S}_i$ is tilted in the z direction and $\mathbf{S}_j$ in the y-direction (i.e., $\delta\mathbf{S}_i = -\delta\theta\,\hat{z}$ and $\delta\mathbf{S}_j = \delta\phi\,\hat{y}$) yielding $J_{ij}^{zy} = \partial^2 H/\partial z_i \partial y_j = -\partial^2 H/\partial\theta_i\partial\phi_j$.

Within the Korringa-Kohn-Rostoker Green function method, one considers the atomic potentials as scattering centers at points $\mathbf{R}_i$, each characterized by a scattering t-matrix $t_i(E)$. A central quantity is the scattering path operator $\tau(E)$, which is connected to the site-dependent scattering t-matrix $t_i(E)$ and to the free-space structure constants $g_{ij}(E)$ via the matrix relation

$$\tau(E) = [\mathsf{t}^{-1}(E) - \mathsf{g}(E)]^{-1} = \mathsf{t} + \mathsf{t}\,\mathsf{g}\,\mathsf{t} + \mathsf{t}\,\mathsf{g}\,\mathsf{t}\,\mathsf{g}\,\mathsf{t} + \cdots\,; \tag{42}$$

i.e., the matrix $\tau(E)$ describes the coherent scattering from all centers i. Here, $\mathsf{t}(E)$ is to be understood as a site-diagonal matrix with element $(\mathsf{t})_{ij} = t_i(E)\delta_{ij}$ ($t_i(E)$ is also a matrix with angular-momentum and spin indexes). The free-space structure constants (describing the electron propagation in the absence of scattering) relate a free spherical wave (a Hankel function), outgoing from a center j , to incoming free spherical waves (Bessel functions) at a center i [49].

The change of the integrated density of states (with respect to free space) due to the scattering centers can be connected to the scattering path operator $\tau(E)$ via Lloyd's formula:

$$\Delta N(E) = \frac{1}{\pi}\mathrm{Im}\mathrm{Tr}\ln\tau(E) \tag{43}$$

(Expressions (42) and (43) hold also when relating a perturbed system to any reference system (not just free space), with $t_i(E)$ describing the scattering with respect to the reference system and $\mathsf{g}(E)$ being the reference system structural Green function.)

Utilizing expressions (41), (42) and (43) we can express the change of free energy under an infinitesimal change in the direction of the magnetic moments at sites i and j, which in turn is expressed via a corresponding change in the t-matrices $t_i(E)$ and $t_j(E)$. We proceed as follows. Firstly we express the rotated inverse t-matrix of atom i in terms of rotation matrices $\mathsf{R}(\delta\theta_i, \delta\phi_i)$, corresponding to an infinitesimal change in the moment direction described by angles $\delta\theta_i$ and $\delta\phi_i$:

$$t_i'^{-1} = \mathsf{R}(\delta\theta_i, \delta\phi_i)\, t_i^{-1}\, \mathsf{R}^\dagger(\delta\theta_i, \delta\phi_i). \tag{44}$$

In the absence of spin-orbit coupling, the rotation matrices act only in spin space and are of the form $\mathsf{R}(\delta\theta_i, \delta\phi_i) = \exp[-(i/\hbar)\alpha_i \hat{\mathbf{n}}(\delta\theta_i, \delta\phi_i)\cdot\boldsymbol{\sigma}/2]$ where α_i is the angle and $\hat{\mathbf{n}}$ is the unit vector expressing the real-space rotation $(\delta\theta_i, \delta\phi_i)$, and $\boldsymbol{\sigma}$ is the Pauli matrix vector; then the equations are simplified, yielding the result of Lichtenstein for the exchange constants J_{ij} [10]. Here, however, spin-orbit coupling is present, so that the rotation affects also the angular momentum part of the t-matrix; thus, $\mathsf{R}(\delta\theta_i, \delta\phi_i) = \exp[-(i/\hbar)\alpha_i \hat{\mathbf{n}}(\delta\theta_i, \delta\phi_i) \cdot (\mathbf{L} + \boldsymbol{\sigma}/2)]$, where $\mathbf{L}$ is the angular momentum operator.

For the calculation of the exchange and DM-interactions we are interested in the change of the free energy up to second order in $\delta\theta_i$ and $\delta\phi_i$. Thus, the partial derivatives of the inverse t-matrix are needed. These can be expressed via the derivatives of the rotation matrices (see eq.(44)), as [48]:

$$t^{-1}_{i\,\theta} \equiv \frac{\partial t^{-1}}{\partial \theta_i} = \frac{\partial \mathsf{R}}{\partial \theta_i} t_i^{-1} \mathsf{R}^\dagger + \mathsf{R}\, t_i^{-1} \frac{\partial \mathsf{R}^\dagger}{\partial \theta_i} \tag{45}$$

$$t^{-1}_{i\,\phi} \equiv \frac{\partial t^{-1}}{\partial \phi_i} = \frac{\partial \mathsf{R}}{\partial \phi_i} t_i^{-1} \mathsf{R}^\dagger + \mathsf{R}\, t_i^{-1} \frac{\partial \mathsf{R}^\dagger}{\partial \phi_i} \tag{46}$$

Let us denote the change of t^{-1} due to the rotation of t_i^{-1} by $\delta\mathsf{t}_i^{-1}$ (this matrix has non-zero elements only at the (i,i) block). An infinitesimal rotation at sites i and j brings a change in the scattering path operator,

$$\tau' = [\mathsf{t}^{-1} + \delta\mathsf{t}_i^{-1} + \delta\mathsf{t}_j^{-1} - \mathsf{g}]^{-1} = \tau\,[1 + (\delta\mathsf{t}_i^{-1} + \delta\mathsf{t}_j^{-1})\,\tau]^{-1}. \tag{47}$$

We are interested in the change of the integrated density of states caused by these rotations. Having in mind Lloyd's formula (43), we expand the logarithm of τ' up to second order:

$$\delta \ln \tau = \ln \tau' - \ln \tau = 1 + (\delta\mathsf{t}_i^{-1} + \delta\mathsf{t}_j^{-1}) - \frac{1}{2}(\delta\mathsf{t}_i^{-1} + \delta\mathsf{t}_j^{-1})\,\tau\,(\delta\mathsf{t}_i^{-1} + \delta\mathsf{t}_j^{-1})\,\tau + \cdots \tag{48}$$

From equations (37-40) it is evident that we seek the quantity $\partial^2 \ln \tau / \partial\theta_i \partial\phi_j$ etc. Then only the cross terms of the last part of eq. (48) survive, i.e., $\frac{1}{2}(\delta\mathsf{t}_i^{-1}\,\tau\,\delta\mathsf{t}_j^{-1}\,\tau + \delta\mathsf{t}_j^{-1}\,\tau\,\delta\mathsf{t}_i^{-1}\,\tau)$. Using the cyclic property of the trace, we obtain

$$\frac{\partial^2}{\partial\theta_i \partial\phi_j} \mathrm{Tr} \ln \tau = \frac{\partial^2}{\partial\theta_i \partial\phi_j} \mathrm{Tr}\,(\mathsf{t}_i^{-1}\,\tau\,\mathsf{t}_j^{-1}\,\tau) = \mathrm{Tr}_L\, t^{-1}_{i\,\theta}\,\tau_{ij}\,t^{-1}_{j\,\phi}\,\tau_{ji}, \tag{49}$$

where in the last part the trace is only over angular momentum indexes (we have used the fact that $\delta\mathsf{t}_i^{-1}$ has nonzero elements only in the (i,i)-block). Similar are the expressions for the other partial second derivatives with respect to angles at both i and j. Combining this with Lloyd's formula (43) and with the free energy expression (42), we arrive at the following equations:

$$\frac{\partial^2 F}{\partial\phi_i \partial\phi_j} = -\frac{1}{\pi} \mathrm{Im} \int^{E_F} dE\, \mathrm{Tr}_L [t^{-1}_{i\,\phi}(E)\,\tau_{ij}(E)\,t^{-1}_{j\,\phi}(E)\,\tau_{ji}(E)] \tag{50}$$

$$\frac{\partial^2 F}{\partial\theta_i \partial\phi_j} = -\frac{1}{\pi} \mathrm{Im} \int^{E_F} dE\, \mathrm{Tr}_L [t^{-1}_{i\,\theta}(E)\,\tau_{ij}(E)\,t^{-1}_{j\,\phi}(E)\,\tau_{ji}(E)] \tag{51}$$

$$\frac{\partial^2 F}{\partial\theta_i \partial\theta_j} = -\frac{1}{\pi} \mathrm{Im} \int^{E_F} dE\, \mathrm{Tr}_L [t^{-1}_{i\,\theta}(E)\,\tau_{ij}(E)\,t^{-1}_{j\,\theta}(E)\,\tau_{ji}(E)] \tag{52}$$

The final step is the connection of the two models (the Hamiltonian (30) and density-functional theory) by making the substitution $F \to H$ in eqs. (50-52). Thus we arrive at expressions describing the Dzyaloshinskii-Moriya interaction constants, using also equations (35) and (38-40). We obtain:

$$D^x_{ij} = -\frac{1}{2\pi}\mathrm{Im}\int^{E_F} dE\,\mathrm{Tr}_L \left[t^{-1}_{i\,\phi}(E)\,\tau_{ij}(E)\,t^{-1}_{j\,\theta}(E)\,\tau_{ji}(E) - t^{-1}_{i\,\theta}(E)\,\tau_{ij}(E)\,t^{-1}_{j\,\phi}(E)\,\tau_{ji}(E)\right]_{\substack{\theta_{i,j}=\frac{\pi}{2}\\ \phi_{i,j}=0}} \tag{53}$$

$$D^y_{ij} = -\frac{1}{2\pi}\mathrm{Im}\int^{E_F} dE\,\mathrm{Tr}_L \left[-t^{-1}_{i\,\phi}(E)\,\tau_{ij}(E)\,t^{-1}_{j\,\theta}(E)\,\tau_{ji}(E) + t^{-1}_{i\,\theta}(E)\,\tau_{ij}(E)\,t^{-1}_{j\,\phi}(E)\,\tau_{ji}(E)\right]_{\substack{\theta_{i,j}=\frac{\pi}{2}\\ \phi_{i,j}=\frac{\pi}{2}}} \tag{54}$$

$$D^z_{ij} = -\frac{1}{2\pi}\mathrm{Im}\int^{E_F} dE\,\mathrm{Tr}_L \left\{\left[t^{-1}_{i\,\theta}(E)\,\tau_{ij}(E)\,t^{-1}_{j\,\theta}(E)\,\tau_{ji}(E)\right]_{\substack{\theta_{i,j}=0\\ \phi_i=0\\ \phi_j=\frac{\pi}{2}}} - \left[t^{-1}_{i\,\theta}(E)\,\tau_{ij}(E)\,t^{-1}_{j\,\theta}(E)\,\tau_{ji}(E)\right]_{\substack{\theta_{i,j}=0\\ \phi_i=\frac{\pi}{2}\\ \phi_j=0}}\right\} \tag{55}$$

5.2 Calculating the DM interaction with periodic spin spirals

An alternative way to obtain model parameters like the elements of the above discussed matrix J_{ij} from first principles is to fit the energy expression obtained from the model ansatz to the total energies obtained from electronic structure calculations for different magnetic states. We follow this strategy in order to obtain the micromagnetic parameters that are discussed in section 4. If we know the orientation of the Dzyaloshinskii vector from symmetry considerations, we can constrain the magnetization to the plane normal to $\mathbf{D}$ and work with equation (22). For homogeneous spin spirals (i.e. spirals with $\dot{\varphi}(x) = q = \text{const}$ or a constant canting angle $\arccos(\mathbf{S}_i{\cdot}\mathbf{S}_{i+1})$ between the magnetizations of two adjacent lattice sites) the magnetic structure has a period of $\lambda_{\text{hs}} = 2\,\pi/q$ and the energy density E/λ_{hs} of the micromagnetic model gets

$$\frac{q}{2\,\pi}\,E(q) = \frac{q}{2\,\pi}\int\limits_0^{\frac{2\,\pi}{q}} \mathrm{d}x\,\left(A\,q^2 + D\,q + K\sin^2(q\,x)\right) = A\,q^2 + D\,q + \tfrac{1}{2}\,K\ . \tag{56}$$

Thus, we can obtain our model parameters A and D from a quadratic and a linear fit to the dispersion curve $q\,E(q)$, with latter obtained from first-principles calculations. In order to determine the anisotropy constant K, we can perform independent calculations of collinear configurations with $\varphi = 0$ and $\varphi = \pi$.

Since the micromagnetic model is valid in the limit of slow spatial rotations, relation (56) holds only for homogeneous spin spirals with large period lengths. This presents a formidable problem, since the size of the unit cell that one can treat is limited by the computing facilities. We employ a perturbative scheme in order to deal with these large magnetic superstructures: In contrast to the method described in the previous section, we calculate the rotations selfconsistently but treat the spin-orbit coupling as a perturbation. Thereby, we make use of the local force theorem [10, 50]. If we neglect spin-orbit coupling, the orientation of the magnetic moments with respect to the crystal lattice is irrelevant and we can calculate the electronic structure of a homogeneous spin spiral within the chemical unit cell by applying a generalized Bloch theorem [51, 52]. The resulting eigenstates of the unperturbed Hamiltonian $\mathcal{H}_0$ have the form

$$\psi_{\mathbf{k},\nu}(\mathbf{r}) = \begin{pmatrix} \psi^{(\uparrow)}_{\mathbf{k},\nu}(\mathbf{r}) \\ \psi^{(\downarrow)}_{\mathbf{k},\nu}(\mathbf{r}) \end{pmatrix} = \exp(i\,\mathbf{k}\cdot\mathbf{r}) \begin{pmatrix} \exp(-i\,\frac{1}{2}\,\mathbf{q}\cdot\mathbf{r})\; u^{(\uparrow)}_{\mathbf{k},\nu}(\mathbf{r}) \\ \exp(+i\,\frac{1}{2}\,\mathbf{q}\cdot\mathbf{r})\; u^{(\downarrow)}_{\mathbf{k},\nu}(\mathbf{r}) \end{pmatrix} \tag{57}$$

with the $\mathbf{q}$-vector of length $|q|$ pointing along the propagation direction of the spiral and the functions $u^{(\uparrow)}_{\mathbf{k},\nu}(\mathbf{r})$, $u^{(\downarrow)}_{\mathbf{k},\nu}(\mathbf{r})$ possessing the period of the chemical lattice. Of course, $\mathbf{k}$ denotes a $\mathbf{k}$-vector of the reciprocal chemical lattice. In a next step, we apply the spin-orbit coupling operator $\mathcal{H}_{\text{so}}$ in second variation, i.e. we expand the eigenfunctions of $\mathcal{H}_0+\mathcal{H}_{\text{so}}$ in eigenfunctions of $\mathcal{H}_0$ and construct the Hamiltonian matrix with the matrix elements $\langle\psi_{\mathbf{k}',\nu'}|\mathcal{H}_0 + \mathcal{H}_{\text{so}}|\psi_{\mathbf{k},\nu}\rangle$. Since we can neglect all states of high energy, this procedure reduces the size of the Hamiltonian matrix drastically. The spin-orbit coupling is well described by

$$\mathcal{H}_{\text{so}} = \sum_{\alpha} \frac{1}{r_\alpha}\,\frac{\mathrm{d}V_\alpha(r_\alpha)}{\mathrm{d}r_\alpha}\;\boldsymbol{\sigma}\cdot\hat{\mathbf{L}}_\alpha = \begin{pmatrix} \mathcal{H}^{(\uparrow,\uparrow)}_{\text{so}} & \mathcal{H}^{(\uparrow,\downarrow)}_{\text{so}} \\ \mathcal{H}^{(\downarrow,\uparrow)}_{\text{so}} & \mathcal{H}^{(\downarrow,\downarrow)}_{\text{so}} \end{pmatrix} \tag{58}$$

where the index α denotes the atoms. Since only the spin-independent part of the potential enters $\mathcal{H}_{\text{so}}$, its real-space representation possesses the period of the chemical lattice. This allows us to write the matrix elements in the form

$$\begin{aligned} \langle\psi^{(\uparrow)}_{\mathbf{k}',\nu'}|\,\mathcal{H}^{(\uparrow,\uparrow)}_{\text{so}}\,|\psi^{(\uparrow)}_{\mathbf{k},\nu}\rangle &= \textstyle\int\!\mathrm{d}\mathbf{r}\;\; \mathrm{e}^{i\,(\mathbf{k}-\mathbf{k}')\cdot\mathbf{r}} \quad u^{(\uparrow,\uparrow)}(\mathbf{r})\;, \\ \langle\psi^{(\uparrow)}_{\mathbf{k}',\nu'}|\,\mathcal{H}^{(\uparrow,\downarrow)}_{\text{so}}\,|\psi^{(\downarrow)}_{\mathbf{k},\nu}\rangle &= \textstyle\int\!\mathrm{d}\mathbf{r}\;\; \mathrm{e}^{i\,(\mathbf{k}-\mathbf{k}'+\mathbf{q})\cdot\mathbf{r}}\; u^{(\uparrow,\downarrow)}(\mathbf{r})\;, \\ \langle\psi^{(\downarrow)}_{\mathbf{k}',\nu'}|\,\mathcal{H}^{(\downarrow,\uparrow)}_{\text{so}}\,|\psi^{(\uparrow)}_{\mathbf{k},\nu}\rangle &= \textstyle\int\!\mathrm{d}\mathbf{r}\;\; \mathrm{e}^{i\,(\mathbf{k}-\mathbf{k}'-\mathbf{q})\cdot\mathbf{r}}\; u^{(\downarrow,\uparrow)}(\mathbf{r})\;, \\ \langle\psi^{(\downarrow)}_{\mathbf{k}',\nu'}|\,\mathcal{H}^{(\downarrow,\downarrow)}_{\text{so}}\,|\psi^{(\downarrow)}_{\mathbf{k},\nu}\rangle &= \textstyle\int\!\mathrm{d}\mathbf{r}\;\; \mathrm{e}^{i\,(\mathbf{k}-\mathbf{k}')\cdot\mathbf{r}} \quad u^{(\downarrow,\downarrow)}(\mathbf{r}) \end{aligned} \tag{59}$$

$$H_{\{\mathbf{k}\}} = \Big(\delta_{\mathbf{k},\mathbf{k}'}\delta_{\nu,\nu'}\,\epsilon_{\mathbf{k},\nu} + \langle\psi_{\mathbf{k},\nu'}|\mathcal{H}_{\text{so}}|\psi_{\mathbf{k},\nu}\rangle \Big)_{\substack{\mathbf{k},\mathbf{k}'\\ \nu,\nu'}} =$$

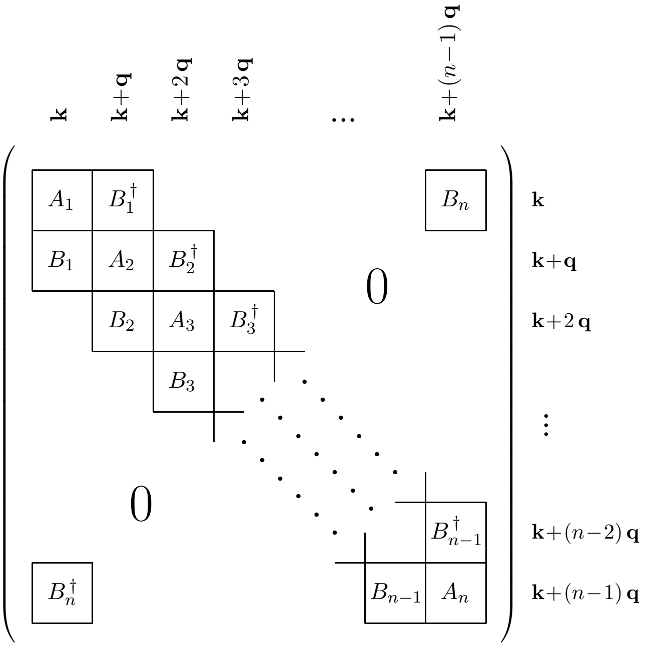

Figure 20: Block of the Hamiltonian matrix for spin-spiral basis functions.

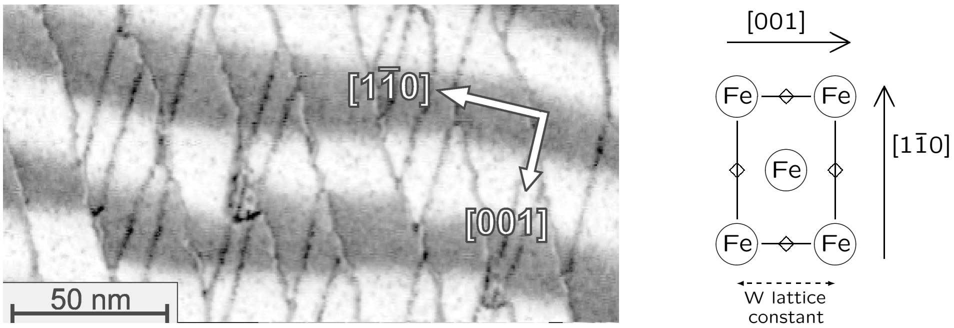

Figure 21: (from [56]) Magnetic domain structure imaged with spin polarized STM. The bright and dark areas correspond to domains with magnetization aligned parallel or antiparallel to the magnetization of the STM tip. The vertical stripes originate from step edges and other geometrical irregularities. The domain walls are oriented normal to the [001]-direction.

with lattice-periodic functions $u^{(\uparrow,\uparrow)}$, $u^{(\uparrow,\downarrow)}$, $u^{(\downarrow,\uparrow)}$, $u^{(\downarrow,\downarrow)}$. Obviously, these matrix elements are non-zero if and only if the exponents are zero. If we choose a **q**-vector that is commensurate with the reciprocal lattice (i.e. a spiral that is commensurate within a certain supercell) and a **k**-grid that is commensurate to the **q**-vector, then we obtain a block-diagonal and sparse Hamiltonian matrix. Each block contains the matrix elements from all **k**-vectors that are connected by **q** (cf. figure 20). Note, that **q** is a reciprocal lattice vector of the large magnetic unit cell in which the spin spiral is commensurate.

For large systems, the Hamiltonian matrix that is shown in figure 20 is too large for straightforward diagonalization. But since we are applying the local force theorem, we only need to know the sum of occupied eigenvalues. This allows to use a perturbative technique that requires exact diagonalization only in a subspace close to the Fermi energy and exploits the sparseness [45].

6 An example: Domain walls in Fe/W(110)

In this section, we illustrate the relevance of the DM interaction by discussing an exemplary system, namely an ultrathin Fe film consisting of two atomic layers grown on the W(110)-surface. We choose this system, since its magnetic structure is elaborately studied by spin-polarized STM, cf. e.g. [53, 54, 55]. A typical STM image is shown in figure 21.

The system shows ferromagnetic domains with the magnetization pointing out-of-plane along the easy axis. The spatial orientation of the corresponding domain walls is determined by the

	K_{001}		$K_{1\bar{1}0}$		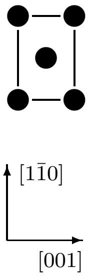
walls normal to [001] A_{001}	⊙ → ⊗ ⊙ → ⊗ ⊙ → ⊗ $+D_{001}$	⊙ ← ⊗ ⊙ ← ⊗ ⊙ ← ⊗ $-D_{001}$	⊙ ↑ ⊗ ⊙ ↑ ⊗ ⊙ ↑ ⊗ $D=0$	⊙ ↓ ⊗ ⊙ ↓ ⊗ ⊙ ↓ ⊗ $D=0$	
walls normal to [1$\bar{1}$0] $A_{1\bar{1}0}$	⊗ ⊗ ⊗ → → → ⊙ ⊙ ⊙ $D=0$	⊗ ⊗ ⊗ ← ← ← ⊙ ⊙ ⊙ $D=0$	⊗ ⊗ ⊗ ↑ ↑ ↑ ⊙ ⊙ ⊙ $+D_{1\bar{1}0}$	⊗ ⊗ ⊗ ↓ ↓ ↓ ⊙ ⊙ ⊙ $-D_{1\bar{1}0}$	

Table 1: Planar rotation paths and corresponding model parameters. In the domains, the magnetization points out-of-plane.

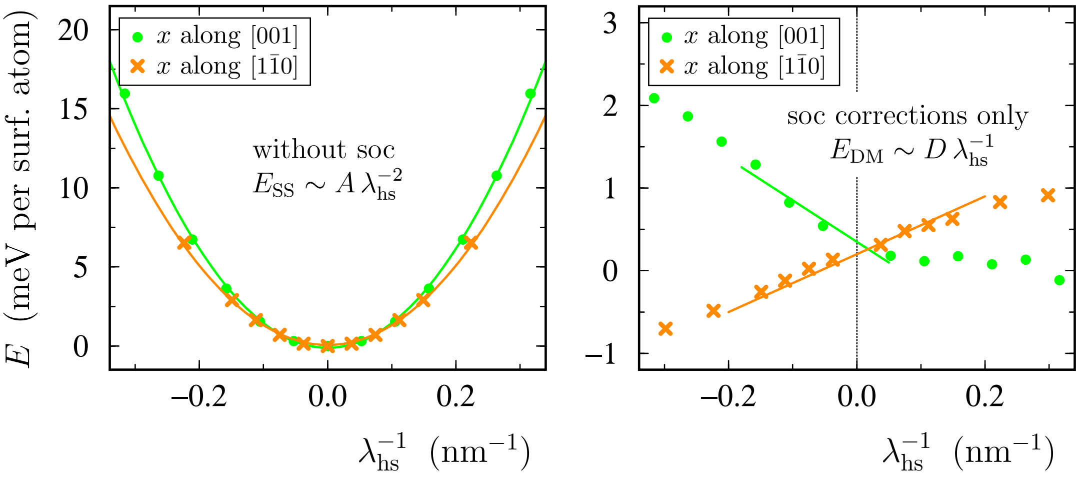

Figure 22: Energies of homogeneous spin spirals obtained from electronic-structure calculations. $|\lambda_{\mathrm{hs}}|$ denotes the spirals period length and the sign of λ_{hs} depends on the rotational direction. The left panel shows the energies obtained by neglecting spin-orbit coupling, quadratic fits to these curves yield the values for A. The right panel shows the effect of the spin-orbit coupling, here we plotted the energy differences between the results obtained by including and neglecting spin-orbit coupling. The spin-rotation axis is chosen in-plane and orthogonal to the propagation direction. The slopes of the curves at $\lambda_{\mathrm{hs}}^{-1} = 0$ correspond to D. The fits are indicated with solid lines.

crystal lattice and hardly influenced by the mesoscopic shape of the sample: The walls are preferably oriented normal to the [001]-direction (i.e. the magnetization changes along [001] and remains constant along [1$\bar{1}$0]). In the following, we want to investigate this effect on the basis of the previously introduced micromagnetic models. If the DM term is irrelevant, the magnetization in the domain walls tries to avoid the hard axis and the magnetization rotation axis does not depend on the propagation direction. In this case, the energies $\sqrt{A\,K}$ of walls that are oriented in different crystallographic directions differ due to the spin stiffness, the value of A depends on the propagation direction. However, the values obtained for A by electronic-structure calculations do not change much for different propagation direction (cf. figure 22 left panel). A further indication of the relevance of the DM interaction in the studied system is the fact, that all domain walls that are observed within one sample show the same rotational direction [57], this cannot be explained on the basis of symmetric exchange interactions. In the following we take the DM term into account, but we restrict our investigations to planar domain walls that can be described with the equations (22) and (26). If the propagation direction and the spin-rotation axis are both oriented along a high-symmetry line, we have to consider eight different walls that depend on six parameters. The walls are listed in table 1 and their energies are given by equation (26).

We estimate values for the model parameters by electronic-structure calculations. These calculations are performed with the FLAPW method implemented in the FLEUR code [12]. A and D are obtained by using a generalized Bloch theorem [51, 52] and the approach introduced in section 5.2. The results of these calculations are shown in figure 22. The anisotropy constant K consists of two main contributions, a term due to the anisotropic electronic energy and a term due to the magnetostatic interactions. The first term can be estimated directly from the electronic energies of collinear configurations with different spin quantization axes, the second term can be estimated from the magnetic (dipole) moments $\mathbf{M}_j$ by applying the well-known formula

$$E^{(\mathrm{dip})} = \frac{\mu_{\mathrm{B}}^2}{2} \sum_{j \neq 0} \frac{(\mathbf{M}_j \cdot \mathbf{M}_0)(\mathbf{R}_j - \mathbf{R}_0)^2 - 3\big((\mathbf{R}_j - \mathbf{R}_0) \cdot \mathbf{M}_j\big)\big((\mathbf{R}_j - \mathbf{R}_0) \cdot \mathbf{M}_0\big)}{|\mathbf{R}_j - \mathbf{R}_0|^5} \; . \tag{60}$$

This sum converges fast, since we are considering a two-dimensional ultrathin magnetic film and not a magnetic bulk system. The results our calculations are summarized in table 2 (for computational details cf. [45]). The values given for the spin-stiffness constants A are fairly accurate, since they are obtained from an unambiguous fitting procedure on a curve on a large energy scale (cf. figure 22). The values given for D are less accurate, but they tell us the order of magnitude of the Dzyaloshinskii vector. The accuracy of the anisotropy constants K is not satisfactory, these calculations reach the limit of our computational method and we cannot rule out an error of a few $\mathrm{meV\,nm^{-1}}$ (note that $1\ \mathrm{meV\,nm^{-2}} \mathrel{\widehat{=}} 0.035$ meV per Fe atom).

		001	$1\bar{1}0$
spin stiffness	A / (meV)	56.4	44.8
DM interaction	D / ($\mathrm{meV\,nm^{-1}}$)	−10.4	7.3
anisotropy energy	K / ($\mathrm{meV\,nm^{-2}}$)	1.1	2.3

Table 2: Theoretically predicted model parameters converted into areal densities. The crystallographic directions refer to the indices used in table 1.

Inserting the values given in table 2 in equation (26) yields the wall energies

$$\begin{aligned}
4\sqrt{A_{001}\,K_{001}} - \pi\,|D_{001}| &= -1.2\ \mathrm{meV\,nm^{-1}} \; , \\
4\sqrt{A_{001}\,K_{1\bar{1}0}} &= 45.6\ \mathrm{meV\,nm^{-1}} \; , \\
4\sqrt{A_{1\bar{1}0}\,K_{001}} &= 28.1\ \mathrm{meV\,nm^{-1}} \; , \\
4\sqrt{A_{1\bar{1}0}\,K_{1\bar{1}0}} - \pi\,|D_{1\bar{1}0}| &= 17.7\ \mathrm{meV\,nm^{-1}} \; .
\end{aligned} \tag{61}$$

A negative wall energy indicates that a rotating spin structure is energetically more favorable than a collinear state. From the results (61) we would predict a spiral propagating along the [001]-direction, thus we would not only explain the experimentally observed domain-wall orientation but also the formation of the regular domain pattern. However, due to the large uncertainties in the values and the restriction to planar spin structures, the good agreement with the experiment may be supported by an accidental cancellation of errors. Nevertheless, the calculations clearly show two points: The observed wall orientation cannot be explained by the spin stiffness alone, and the DM interaction is strong enough to compete with the other quantities. Keeping in mind that all domain walls show the same rotational direction, the DM interaction presents the most plausible explanation for the observed mesoscale magnetic structure. The studied system nicely illustrates the relevance of the Dzyaloshinskii-Moriya interactions for magnetic surfaces.

Acknowledgements

We want to thank E. Chulkov and Th. Schäpers for stimulating discussions and acknowledge financial support from Deutsche Forschunsgemeinschaft (DFG) grant No. BI 823/1.

References

[1] M. N. Baibich, J. M. Broto, A. Fert, F. N. V. Dau, F. Petroff, P. Eitenne, G. Creuzet, A. Friederich, and J. Chazelas, Giant magnetoresistance of (001)Fe/(001)Cr magnetic superlattices, Phys. Rev. Lett. **61**, 2472 (1988).

[2] G. Binash, P. Grünberg, F. Saurenbach, and W. Zinn, Enhanced magnetoresistance in layered magnetic structures with antiferromagnetic interlayer exchange, Phys. Rev. B **39**, 4828 (1989).

[3] S. A. Wolf, D. D. Awschalom, R. A. Buhrman, J. M. Daughton, S. von Molnár, M. L. Roukes, A. Y. Chtchelkanova, and D. M. Treger, Spintronics: A spin-based electronic vision for the future, Science **294**, 1488 (2001).

[4] I. Žutć, J. Fabian, and S. D. Sarma, Spintronics: Fundamentals and applications, Rev. Mod. Phys. **76**, 323 (2004).

[5] E. I. Rashba, Properties of semiconductors with an extremum loop, Sov. Phys. Solid State **2**, 1109 (1960).

[6] S. Datta and B. Das, Electronic analog of the electro-optic modulator, Appl. Phys. Lett. **56**, 665 (1990).

[7] W. Heisenberg, Zur Theorie des Ferromagnetismus, Z. f. Physik **49**, 619 (1928).

[8] I. E. Dzialoshinskii, Thermodynamic Theory of "Weak" Ferromagnetism In Antiferromagnetic Substances, Sov. Phys. JETP **5**, 1259 (1957).

[9] T. Moriya, Anisotropic Superexchange Interaction and Weak Ferromagnetism, Physical Review **120**, 91–98 (1960).

[10] A. I. Liechtenstein, M. I. Katsnelson, V. P. Antropov, and V. A. Gubanov, Local spin density functional approach to the theory of exchange interactions in ferromagnetic metals and alloys, J. Magn. Magn. Mater. **67**, 65 (1987).

[11] E. Wimmer, H. Krakauer, M. Weinert, and A. Freeman, Full-potential self-consistent linearized-augmented-plane-wave method for calculating the electronic structure of molecules and surfaces: O_2 molecule, Phys. Rev. B **24**, 864 (1981).

[12] For program description see *http://www.flapw.de.*

[13] C. Li, A. J. Freeman, H. J. F. Jansen, and C. L. Fu, Magnetic anisotropy in low-dimensional ferromagnetic systems: Fe monolayers on Ag(001), Au(001), and Pd(001) substrates, Phys. Rev. B **42**, 5433 (1990).

[14] P. Kurz, F. Förster, L. Nordström, G. Bihlmayer, and S. Blügel, *Ab initio* treatment of noncollinear magnets with the full-potential linearized augmented planewave method, Phys. Rev. B **69**, 024415 (2004).

[15] T. Schäpers, J. Knobbe, and V. A. Guzenko, Effect of Rashba spin-orbit coupling on magnetotransport in InGaAs/InP quantum wire structures, Phys. Rev. B **69**, 235323 (2004).

[16] Y. A. Bychkov and E. I. Rashba, Oscillatory effects and the magnetic-susceptibility of carriers in inversion-layers, J. Phys. C **17**, 6039 (1984).

[17] Y. A. Bychkov and E. I. Rashba, Properties of a 2D electron-gas with lifted spectral degeneracy, Sov. Phys. JETP Lett **39**, 78 (1984).

[18] R. Winkler, Rashba splitting in two-dimensional electron and hole systems, Phys. Rev. B **62**, 4245 (2000).

[19] G. Dresselhaus, Spin-orbit coupling effects in zinc blende structures, Phys. Rev. **100**, 580 (1955).

[20] V. A. Guzenko, J. Knobbe, H. Hardtdegen, T. Schäpers, and A. Bringer, Rashba effect in InGaAs/InP parallel quantum wires, Appl. Phys. Lett. **88**, 032102 (2006).

[21] J. Wróbel, T. Dietl, A. Łusakowski, G. Grabecki, K. Fronc, R. Hey, K. H. Ploog, and H. Shtrikman, Spin Filtering in a Hybrid Ferromagnetic-Semiconductor Microstructure, Phys. Rev. Lett. **93**, 246601 (2004).

[22] S. LaShell, B. A. McDougall, and E. Jensen, Spin Splitting of an Au(111) Surface State Band Observed with Angle Resolved Photoelectron Spectroscopy, Phys. Rev. Lett. **77**, 3419 (1996).

[23] M. Hoesch, M. Muntwiler, V. N. Petrov, M. Hengsberger, L. Patthey, M. Shi, M. Falub, T. Greber, and J. Osterwalder, Spin structure of the Shockley surface state on Au(111), Phys. Rev. B **69**, 241401(R) (2004).

[24] J. Henk, A. Ernst, and P. Bruno, Spin polarization of the L-gap surface states on Au(111), Phys. Rev. B **68**, 165416 (2003).

[25] G. Nicolay, F. Reinert, S. Hüfner, and P. Blaha, Spin-orbit splitting of the L-gap surface state on Au(111) and Ag(111), Phys. Rev. B **65**, 033407 (2001).

[26] G. Bihlmayer, Y. M. Koroteev, P. M. Echenique, E. V. Chulkov, and S. Blügel, The Rashba-effect at metallic surfaces, Surf. Sci. **600**, 3888 (2006).

[27] L. Petersen and P. Hedegård, A simple tight-binding model of spin-orbit splitting of *sp*-derived surface states, Surf. Sci. **459**, 49 (2000).

[28] S. Agergaard, C. Søndergaard, H. Li, M. B. Nielsen, S. V. Hoffmann, Z. Li, and P. Hofmann, The effect of reduced dimensionality on a semimetal: the electronic structure of the Bi(110) surface, New J. Phys. **3**, 15 (2001).

[29] J. Sun, A. Mikkelsen, M. F. Jensen, Y. M. Koroteev, G. Bihlmayer, E. V. Chulkov, D. L. Adams, P. Hofmann, and K. Pohl, Structural determination of the Bi(110) semimetal surface by LEED analysis and *ab initio* calculations, Phys. Rev. B **74**, accepted (2006).

[30] C. R. Ast and H. Höchst, Fermi surface of Bi(111) measured by photoemission spectroscopy, Phys. Rev. Lett. **87**, 177602 (2001).

[31] H. Mönig, J. Sun, Y. M. Koroteev, G. Bihlmayer, E. V. Chulkov, K. Pohl, and P. Hofmann, The structure of the (111) surface of bismuth, Phys. Rev. B **72**, 085410 (2005).

[32] J. I. Pascual, G. Bihlmayer, Y. M. Koroteev, H.-P. Rust, G. Ceballos, M. Hansmann, K. Horn, E. V. Chulkov, S. Blügel, P. M. Echenique, and P. Hofmann, The role of the spin in quasiparticle interference, Phys. Rev. Lett. **93**, 196802 (2004).

[33] P. Hofmann, J. E. Gayone, G. Bihlmayer, Y. M. Koroteev, and E. V. Chulkov, Electronic structure and Fermi surface of Bi(100), Phys. Rev. B **71**, 195413 (2005).

[34] Y. M. Koroteev, G. Bihlmayer, J. E. Gayone, E. V. Chulkov, S. Blügel, P. M. Echenique, and P. Hofmann, Strong spin-orbit splitting on Bi surfaces, Phys. Rev. Lett. **93**, 046403 (2004).

[35] C. R. Ast and H. Höchst, Indication of charge-density-wave formation in Bi(111), Phys. Rev. Lett. **90**, 016403 (2003).

[36] T. Hirahara, T. Nagao, I. Matsuda, G. Bihlmayer, E. V. Chulkov, Y. M. Koroteev, P. M. Echenique, M. Saito, and S. Hasegawa, Role of spin-orbit coupling and hybridization effects in the electronic structure of ultrathin Bi films, Phys. Rev. Lett. **97**, 146803 (2006).

[37] O. Krupin, G. Bihlmayer, K. Starke, S. Gorovikov, J. E. Prieto, K. Döbrich, S. Blügel, and G. Kaindl, Rashba effect at magnetic metal surfaces, Phys. Rev. B **71**, 201403 (R) (2005).

[38] D. A. Smith, New mechanisms for magnetic anisotropy in localised s-state moment materials, J. Magn. Magn. Mater. **1**, 214 (1976).

[39] A. Fert and P. M. Levy, Role of Anisotropic Exchange Interactions in Determining the Properties of Spin-Glasses, Phys. Rev. Lett. **44**, 1538 (1980).

[40] U. K. Rößler, A. N. Bogdanov, and C. Pfleiderer, Spontaneous skyrmion ground states in magnetic metals, Nature **442**, 797 (2006).

[41] C. Kittel, Physical Theory of Ferromagnetic Domains, Rev. Mod. Phys. **49**, 541 (1949).

[42] I. E. Dzyaloshinskiĭ, Theory of helicoidal structures in antiferromagnets. III., Sov. Phys. JETP **20**, 665 (1965).

[43] Yu. A. Izyumov, Modulated, or long-periodic, magnetic structures of crystals, Sov. Phys. Usp. **27**, 845 (1984).

[44] L. Landau and E. Lifshitz, On the Theory of the Dispersion of Magnetic Permeability in Ferromagnetic Bodies, Phys. Z. Sowjetunion **8**, 153 (1935).

[45] M. Heide, Magnetic domain walls in ultrathin films: Contribution of the Dzyaloshinsky-Moriya interaction, PhD Thesis, RWTH Aachen, Germany, 2006.

[46] M. Heide, G. Bihlmayer, and S. Blügel, to be published.

[47] J. B. Staunton, B. L. Gyorffy, J. Poulter, and P. Strange, A relativistic RKKY interaction between two magnetic impurities-the origin of a magnetic anisotropic effect, J. Phys. C: Solid State Phys. **21**, 1595 (1988).

[48] L. Udvardi, L. Szunyogh, K. Palotas, and P. Weinberger, First-principles relativistic study of spin waves in thin magnetic films, Phys. Rev. B **68**, 104436 (2002).

[49] A. Gonis, *Theoretical Materials Science*, Materials Research Society, 2000.

[50] A. R. Mackintosh and O. K. Andersen, *Electrons at the Fermi Surface*, page 149, ed. M. Springford, Cambridge Univ. Press, London, 1980.

[51] C. Herring, *Exchange interactions among intinerant electrons, Magnetism Vol. IV*, ed. G. T. Rado, H. Suhl, Academic Press, New York, London, 1966.

[52] L. M. Sandratskii, Symmetry analysis of electronic states for crystals with spiral magnetic order. I. General properties, J. Phys.: Condens. Matter **3**, 8565 (1991).

[53] M. Pratzer, H. J. Elmers, M. Bode, O. Pietzsch, A. Kubetzka, and R. Wiesendanger, Atomic-scale magnetic domain walls in quasi-one-dimensional Fe nanostripes, Phys. Rev. Lett. **87**, 127201 (2001).

[54] M. Bode, Spin-polarized scanning tunneling microscopy, Rep. Prog. Phys. **66**, 523 (2003).

[55] E. Y. Vedmedenko, A. Kubetzka, K. von Bergmann, O. Pietzsch, M. Bode, J. Kirschner, H. P. Oepen, and R. Wiesendanger, Domain Wall Orientation in Magnetic Nanowires, Phys. Rev. Lett. **92**, 77207 (2004).

[56] K. von Bergmann, Iron nanostructures studied by spin-polarized scanning tunneling microscopy, PhD Thesis, Universität Hamburg, Germany, 2004.

[57] O. Pietzsch, Magnetic Imaging by Spin-Polarized Scanning Tunneling Spectroscopy Applied to Ultrathin Fe/W(110) Films, PhD Thesis, Universität Hamburg, Germany, 2001.